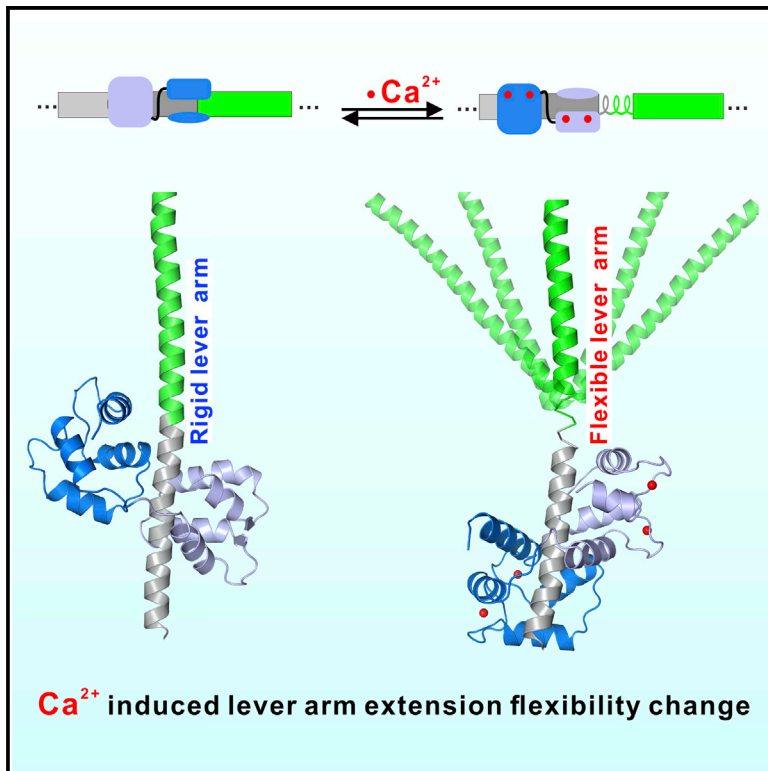


# Structure

## Ca<sup>2+</sup>-Induced Rigidity Change of the Myosin VIIa IQ Motif-Single $\alpha$ Helix Lever Arm Extension

### Graphical Abstract



### Authors

Jianchao Li, Yiyun Chen, Yisong Deng, Ilona Christy Unarta, Qing Lu, Xuhui Huang, Mingjie Zhang

### Correspondence

bcjli@connect.ust.hk (J.L.),  
mzhang@ust.hk (M.Z.)

### In Brief

The structures of Myo7a IQ5-SAH lever arm extension in complex with apo- and Ca<sup>2+</sup>-CaM, respectively, reveal that the motor contains an extended and rigid lever arm at low Ca<sup>2+</sup> concentration conditions. Increased cellular Ca<sup>2+</sup> concentration induces conformational flexibility of the motor and thus regulates its activity.

### Highlights

- Myo7a contains a stable single  $\alpha$  helix (SAH) following its IQ motifs
- Apo-CaM stabilizes the conformational rigidity of the IQ5-SAH lever arm extension
- Ca<sup>2+</sup> increases flexibility of the IQ5-SAH lever arm extension of Myo7a
- Ca<sup>2+</sup>-induced lever arm flexibility change may also occur in other myosins



# Ca<sup>2+</sup>-Induced Rigidity Change of the Myosin VIIa IQ Motif-Single $\alpha$ Helix Lever Arm Extension

Jianchao Li,<sup>1,5,\*</sup> Yiyun Chen,<sup>1,5</sup> Yisong Deng,<sup>1,6</sup> Ilona Christy Unarta,<sup>2</sup> Qing Lu,<sup>1,3,4</sup> Xuhui Huang,<sup>2,3</sup> and Mingjie Zhang<sup>1,3,4,7,\*</sup>

<sup>1</sup>Division of Life Science, State Key Laboratory of Molecular Neuroscience, Hong Kong University of Science and Technology, Clear Water Bay, Kowloon, Hong Kong, China

<sup>2</sup>Department of Chemistry, Hong Kong University of Science and Technology, Clear Water Bay, Kowloon, Hong Kong, China

<sup>3</sup>Center of Systems Biology and Human Health, Hong Kong University of Science and Technology, Clear Water Bay, Kowloon, Hong Kong, China

<sup>4</sup>Institute for Advanced Study, Hong Kong University of Science and Technology, Clear Water Bay, Kowloon, Hong Kong, China

<sup>5</sup>Co-first author

<sup>6</sup>Present address: Department of Integrative Computational and Structural Biology, The Scripps Research Institute, La Jolla, CA 92037, USA

<sup>7</sup>Lead contact

\*Correspondence: [bcjli@connect.ust.hk](mailto:bcjli@connect.ust.hk) (J.L.), [mzhang@ust.hk](mailto:mzhang@ust.hk) (M.Z.)

<http://dx.doi.org/10.1016/j.str.2017.02.002>

## SUMMARY

Several unconventional myosins contain a highly charged single  $\alpha$  helix (SAH) immediately following the calmodulin (CaM) binding IQ motifs, functioning to extend lever arms of these myosins. How such SAH is connected to the IQ motifs and whether the conformation of the IQ motifs-SAH segments are regulated by Ca<sup>2+</sup> fluctuations are not known. Here, we demonstrate by solving its crystal structure that the predicted SAH of myosin VIIa (Myo7a) forms a stable SAH. The structure of Myo7a IQ5-SAH segment in complex with apo-CaM reveals that the SAH sequence can extend the length of the Myo7a lever arm. Although Ca<sup>2+</sup>-CaM remains bound to IQ5-SAH, the Ca<sup>2+</sup>-induced CaM binding mode change softens the conformation of the IQ5-SAH junction, revealing a Ca<sup>2+</sup>-induced lever arm flexibility change for Myo7a. We further demonstrate that the last IQ motif of several other myosins also binds to both apo- and Ca<sup>2+</sup>-CaM, suggesting a common Ca<sup>2+</sup>-induced conformational regulation mechanism.

## INTRODUCTION

Unconventional myosins are actin-based molecular motors that function in cell motility and intracellular transportation (Hartman et al., 2011). Myosin VIIa (Myo7a), a member of the class VII unconventional myosins (Myo7) encoded by *myo7a*, plays essential roles in both the development and physiological functions of the auditory and visual systems in mammals. In the auditory system, Myo7a, together with its associated proteins, is essential for the development and structural maintenance of stereocilia, which are actin-based protrusions at the apical surface of cochlear and vestibular hair cells of inner ears responsible for sound perceptions and spatial balancing (Gillespie and Muller, 2009; Lefevre et al., 2008; Pan and Zhang, 2012; Richardson et al., 2011;

Tilney et al., 1992). In the visual system, Myo7a is expressed in photoreceptor cells and pigmented epithelial cells, and is essential for proper connecting cilium formation as well as melanosome transportation in photoreceptors (Liu et al., 1997a, 1998). Mutations of *myo7a* can cause various human genetic disorders such as Usher syndrome type IB (USH1B), characterized by combined early-onset deafness and blindness (Gibson et al., 1995; Well et al., 1995), and non-syndromic deafness (DFNA11 and DFNB2) (Liu et al., 1997b; Tamagawa et al., 1996; Weil et al., 1997). Numerous Myo7a mutations have been identified in patients, and many of these mutations can alter its structural stability or affect its interactions with binding partners (Pan and Zhang, 2012; Wu et al., 2011).

From its N to C terminus, Myo7a contains a motor domain, five calmodulin (CaM) binding IQ motifs, a highly charged post-IQ region predicted to form a single  $\alpha$  helix (SAH), and two MyTH4-FERM tandems separated by an SH3 domain (Figure 1A). In vertebrates, there are two isoforms of Myo7, namely Myo7a and Myo7b, which share a highly similar structural architecture because of their >50% amino acid sequence identity (Chen et al., 2001). Analogous to Myo7a, Myo7b is essential for the formation and maintenance of microvilli in intestinal and kidney brush borders, another type of actin-rich protrusion analogous to stereocilia (Crawley et al., 2014, 2016; Li et al., 2016). Myo7b differs from Myo7a by possessing a short insertion in its motor domain, which may promote its actin binding (Henn and De La Cruz, 2005). Myo7b also lacks a highly charged SAH fragment in its post-IQ region (Figure 1A).

Initially, the highly charged post-IQ region in Myo7a was predicted to be a coiled coil and thought to mediate Myo7a dimerization (Chen et al., 2001). However, a study published a few years later showed that a similar highly charged region directly after the last IQ motif in Myosin X (Myo10) forms a stable SAH and functions to elongate the lever arm of the motor (Knight et al., 2005). Subsequently, it was discovered that Myosin VI (Myo6) also contains a similar charged SAH in its lever arm extension region (Peckham, 2011; Spink et al., 2008). Myo7a is also predicted to contain an SAH-like structure, like a number of non-myosin proteins such as inner centromere protein and caldesmon-1 (Peckham and Knight, 2009; Swanson and

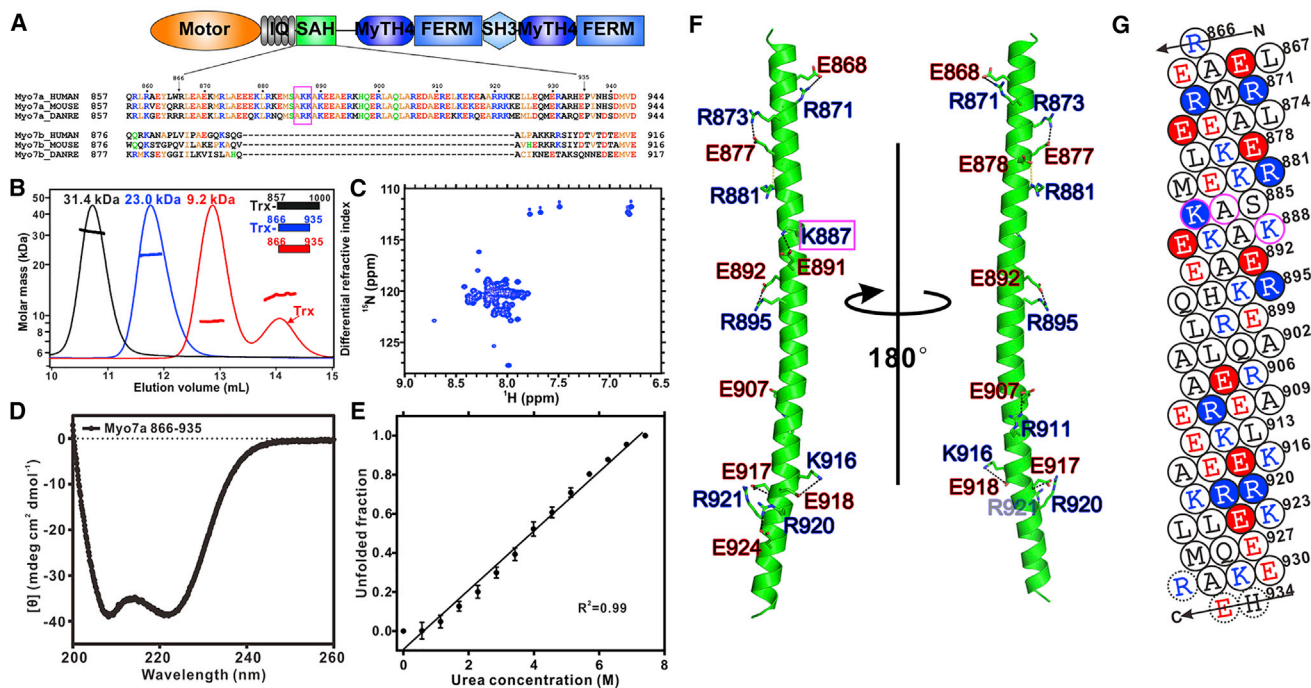


**Figure 1. Myo7a Post-IQ Region Forms a Stable SAH**

(A) Domain organization of Myo7a and sequence alignment of the post-IQ regions of Myo7a and Myo7b. The 3-residue in-frame deletion found in DFNA11 patients is highlighted with a box in magenta.

(B) FPLC-SLS showing that Myo7a post-IQ is monomeric in solution. The experimentally determined molar masses of Trx-Myo7a-857-1000, Trx-Myo7a-866-935, and Myo7a-866-935 were 31.4, 23.0, and 9.2 kDa, which fitted well with their respective theoretical molar masses of 31.8, 23.4, and 9.2 kDa.

(C)  $^{15}\text{N}$ -HSQC spectrum of Myo7a-866-935.

(D) Circular dichroism spectrum of Myo7a-866-935.

(E) Urea-induced denaturation profile of Myo7a-866-935. The change of ellipticity value of the protein at 222 nm was used to calculate the relative fraction of protein denaturation at each urea concentration. Values are means  $\pm$  SD from three independent measurements.

(F) Ribbon diagram of the crystal structure of Myo7a-866-935 with ionic interactions between charged residues labeled. The magenta box highlights K887, which is deleted in the DFNA11 mutation.

(G) Helical net diagrams of Myo7a-866-935. The residues involved in the ionic interactions are highlighted with filled circles. The 3-residue in-frame deletion in DFNA11 patients is highlighted by magenta circles. The C-terminal three residues missing in the electron density are shown in dashed circles.

Sivaramakrishnan, 2014). However, whether the post-IQ region of Myo7a indeed forms an SAH is still being debated. It was recently suggested that part of the Myo7a post-IQ forms a coiled-coil dimer (Sakai et al., 2015).

CaM, as a common light chain of unconventional myosins, is widely known to be critical for the motors to function properly in a  $\text{Ca}^{2+}$ -regulated manner (Bahler and Rhoads, 2002; Batters and Veigel, 2016; Cheney and Mooseker, 1992; Heissler and Sellers, 2014; Trybus, 1994). It is commonly accepted that CaM, in its  $\text{Ca}^{2+}$ -free state, specifically binds to and thereby maintains the conformational rigidity of the IQ motifs (Houdusse et al., 2006; Lu et al., 2015). The apo-CaM-bound IQ motifs serve as lever arms of myosins both in their dimeric transport competent forms and in their monomeric mechanical tethering forms (Heissler and Sellers, 2014; Houdusse et al., 2006). It is also generally perceived that an increase in cellular  $\text{Ca}^{2+}$  concentration will weaken the interaction between CaM and IQ motifs and thereby cause CaM to dissociate from myosins, with subsequent softening of the lever arms of the motors (Heissler and Sellers, 2014; Lu et al., 2015). It should be pointed out that a few IQ motifs in several myosins have been shown to bind to

apo- and  $\text{Ca}^{2+}$ -CaM (Lu et al., 2012b, 2015; Sakai et al., 2015; Zhu et al., 1998). However, structural studies of IQ/ $\text{Ca}^{2+}$ -CaM have been limited to IQ motifs from non-myosin proteins (Chen et al., 2014; Kim et al., 2008; Mori et al., 2008; Van Petegem et al., 2005; Wang et al., 2014).

In this work we solved the crystal structure of the Myo7a post-IQ region, which reveals that it indeed forms a stable SAH. We further determined the crystal structure of IQ5-SAH in complex with apo-CaM. The complex structure, together with biochemical experiments, reveals that the bound apo-CaM plays a critical role in maintaining the conformational rigidity in the junctional region connecting IQ5 and SAH of Myo7a. We discovered that  $\text{Ca}^{2+}$ -CaM remains stably bound to IQ5. The crystal structure of IQ5/ $\text{Ca}^{2+}$ -CaM complex reveals that, upon binding to  $\text{Ca}^{2+}$ , CaM undergoes a translocation along the IQ motifs toward the N terminus of Myo7a by  $\sim 2.5$  helical turns, a movement that causes the IQ5-SAH junction to be completely solvent accessible. As a result, the conformational rigidity of IQ5-SAH (i.e., the lever arm extension) of Myo7a decreases. We further showed that IQ motifs situated at the distal end of several myosin lever arms also bind to both apo- and  $\text{Ca}^{2+}$ -CaM. Finally, we

demonstrated that the missense DFNA11 R853C mutation of Myo7a disrupts the IQ5/apo-CaM interaction and causes functional impairments of the motor.

## RESULTS

### Myo7a Post-IQ Region Forms a Stable SAH

The post-IQ region of Myo7a is evolutionarily conserved (Figure 1A) and shares a charge distribution pattern similar to that of Myo10 SAH. To test whether the post-IQ region of Myo7a may also form a stable SAH instead of a coiled-coil dimer, we first purified a Trx-tagged fragment of mouse Myo7a spanning Arg857 (directly after the last IQ motif) to Lys1000 (the beginning of the first MyTH4 domain). Analytical gel filtration chromatography coupled with static light-scattering (FPLC-SLS) analysis showed that the entire Myo7a post-IQ forms a stable monomer in solution (Figure 1B, fitted molecular weight 31.4 kDa versus theoretical molecular weight 31.8 kDa). We mapped the Myo7a post-IQ to a shorter and stable monomer spanning residues 866–935 (denoted Myo7a-866-935) based on its sequence conservation and secondary structure prediction (Figure 1B). It is noted that the 9.2-kDa Myo7a-866-935 after Trx-tag cleavage was eluted at a smaller volume than the 14-kDa Trx tag, indicating that Myo7a-866-935 adopts an elongated shape instead of the globular Trx (Figure 1B). The  $^{15}\text{N}$ -heteronuclear single-quantum coherence (HSQC) spectrum of the  $^{15}\text{N}$ -labeled Myo7a-866-935 showed that the majority of the backbone peaks are distributed in a narrow chemical-shift window typical for  $\alpha$ -helical conformation (Figure 1C). Consistently, the circular dichroism (CD) spectrum of Myo7a-866-935 showed that the protein is largely  $\alpha$ -helical (Figure 1D). We next performed a denaturation experiment of Myo7a-866-935 by monitoring the ellipticity of the protein at 222 nm as a function of increasing urea concentrations. It is noteworthy that the decreasing of the helical content of the protein is linearly proportional to increasing urea concentration ( $R^2 = 0.99$ ), indicating that Myo7a-866-935 is stably folded but does not contain any tertiary structure (Figure 1E). Taken together, the above biophysical characterizations strongly indicate that Myo7a-866-935 forms a stable monomer enriched in  $\alpha$ -helical conformation.

To gain further insight, we determined the crystal structure of Myo7a-866-935 at 2.1-Å resolution (Table 1 and Figure 1F). The structure was solved by a combination of single-wavelength anomalous dispersion of iodide derivatives of sample crystals and molecular replacement methods. All of Myo7a-866-935 except for the C-terminal three residues (933–935) are visible in the electron density, and the protein forms a straight, rigid SAH. A total of eight pairs of E-R/K charge-charge interactions are distributed throughout the entire helix (Figures 1F and 1G), which presumably are the key determinants for the stable  $\alpha$ -helix formation of SAH in Myo7a as well as Myo10 (Knight et al., 2005). Human genetics studies have identified a 9-bp deletion within exon 22 of *myo7a*, resulting in an in-frame deletion of Ala886, Lys887, and Lys888 from Myo7a, and the mutation is known to cause non-syndromic deafness DFNA11 in patients (Liu et al., 1997c). From the Myo7a-866-935 structure, Lys887 forms a charge-charge interaction with Glu891 (Figures 1F and 1G). The deletion of the three residues containing Lys887 is likely to destabilize SAH, which might impair the function of Myo7a in the patients.

### IQ5 and SAH Form a Continuous Helix in the Presence of Apo-CaM

Single-molecule experiments have shown that by replacing part of the IQ motif-based lever arm with a similar length of SAH, Myosin-Va (Myo5a) can still processively move on actin filaments (Baboolal et al., 2009), indicating that SAH can function to extend the lever arm length of myosins. To function as a lever arm extension of a myosin, the SAH segment of the motor must be connected to its IQ motif helix, forming a rigid structural entity (i.e., a continuous and stable  $\alpha$  helix), so that the mechanical force produced by the motor head can be transmitted through the entire lever arm. To test this hypothesis, we set out to determine the crystal structure of IQ5-SAH in complex with apo-CaM. Using a boundary with residues 834–935 of mouse Myo7a (referred to as Myo7a-IQ5-SAH) and by co-expressing with CaM, we succeeded in purifying a stable Myo7a-IQ5-SAH/CaM complex in the presence of EDTA in the sample buffer and obtained complex crystals that diffracted to 3.0-Å resolution (Table 1). The structure of the Myo7a-IQ5-SAH/CaM complex was solved by the molecular replacement method using the Myo5a-IQ1/apo-CaM complex structure (PDB: 2IX7) and the Myo7a SAH structure determined above as the search models. Indeed, IQ5 is bound by apo-CaM in a canonical fashion, with the C-terminal lobe of CaM adopting a semi-open conformation and the N lobe adopting a closed conformation (Figure S1) (Houdusse et al., 2006). Importantly, SAH follows directly after IQ5, together forming one continuous and rigid  $\alpha$  helix (Figure 2A). The electron density ( $2F_o - F_c$  map, contoured at  $1\sigma$ ) of the junctional region between IQ5 and SAH clearly showed that the C-terminal tail of IQ5 and the beginning of SAH form a continuous and regular  $\alpha$ -helical structure, and the N-terminal lobe of apo-CaM intimately contacts with several residues from the junctional region between IQ5 and SAH (Figure 2B). The interaction between very negatively charged CaM and the positively charged IQ5/SAH junction is likely to be important for the structural stability of the IQ5-SAH helix, as otherwise unfavorable repulsions resulted from two pairs of positively charged residues in the junctional region (Arg854-Arg858 and Arg853-His856, Figure 2B) would distort the helix formation (see below for more details). Supporting this, in the recently solved crystal structure of Myo10 SAH together with the antiparallel coiled coil (Myo10-SAH-antiCC), although half of the IQ3 was included in the crystallization construct, the absence of apo-CaM binding made it partially disordered (Ropars et al., 2016). It is generally accepted that tandem IQ motifs can form a continuous helix in the presence of apo-CaM in unconventional myosins (Houdusse et al., 2006; Lu et al., 2015). As such, the five IQ motifs of Myo7a contribute to a lever arm length of  $\sim 19$  nm and the SAH further extends the lever arm by  $\sim 9$  nm, rendering the motor to have a total lever arm length of  $\sim 28$  nm (Figure 2A).

The continuous helix formation in Myo7a-IQ5-SAH provides a mechanistic basis for SAH to act as a lever arm extension of the motor. The regular distribution of charged residues is the characteristic of SAH, and an algorithm to predict the existence of SAH has been developed (Gaspari et al., 2012). We set out to search for the possible presence of SAH in all myosins using this method. For all myosins in the mouse proteome deposited in Swiss-Prot (UniProt Consortium, 2015), only Myo7a, Myo10,

**Table 1. X-Ray Crystallographic Data Collection and Model Refinement**

Data Collection				
Datasets	866-935-Native	866-935-KI	IQ5-SAH/Apo-CaM	IQ5/Ca <sup>2+</sup> -CaM
Space group	<i>P</i> 2 <sub>1</sub>	<i>C</i> 2	<i>P</i> 4 <sub>1</sub>	<i>P</i> 2 <sub>1</sub>
Wavelength (Å)	0.9793	1.5418	1.0300	0.9791
Unit cell parameters (Å)	<i>a</i> = 38.81, <i>b</i> = 42.61, <i>c</i> = 59.68 $\alpha = \gamma = 90^\circ$ , $\beta = 90.07^\circ$	<i>a</i> = 49.06, <i>b</i> = 38.79, <i>c</i> = 45.44 $\alpha = \gamma = 90^\circ$ , $\beta = 99.78^\circ$	<i>a</i> = <i>b</i> = 80.93, <i>c</i> = 175.29 $\alpha = \beta = \gamma = 90^\circ$	<i>a</i> = 38.68, <i>b</i> = 89.76, <i>c</i> = 45.72 $\alpha = \gamma = 90^\circ$ , $\beta = 106.03^\circ$
Resolution range (Å)	50–2.10 (2.21–2.10)	50–2.70 (2.85–2.70)	50–3.0 (3.16–3.00)	50–2.35 (2.39–2.35)
No. of unique reflections	11,455 (1,683)	2,393 (356)	22,489 (3,279)	12,459 (622)
Redundancy	3.4 (3.5)	6.6 (6.5)	6.7 (6.9)	2.8 (2.7)
<i>I</i> / $\sigma$	8.3 (2.0)	10.6 (3.9)	9.3 (2.0)	23.0 (4.1)
Completeness (%)	99.0 (99.5)	100 (100)	99.6 (100)	97.5 (98.9)
<i>R</i> <sub>merge</sub> <sup>a</sup> (%)	8.8 (61.8)	12.2 (43.6)	13.1 (96.7)	6.2 (36.0)
Structure Refinement				
Resolution (Å)	50–2.1 (2.31–2.10)		50–3.0 (3.08–3.00)	50–2.35 (2.56–2.35)
<i>R</i> <sub>cryst</sub> <sup>b</sup> / <i>R</i> <sub>free</sub> <sup>c</sup> (%)	19.46/23.85 (27.87/29.95)		22.37/29.01 (30.62/34.11)	22.73/27.06 (29.40/32.66)
Rmsd bonds (Å)/angles (°)	0.010/1.071		0.006/0.939	0.013/1.153
Average <i>B</i> factor <sup>d</sup>	40.4		102.3	45.4
No. of atoms				
Protein atoms	1,198		3,104	2,472
Other molecules	7		0	35
No. of reflections				
Working set	10,868		20,428	11,838
Test set	548		2002	598
Ramachandran plot regions <sup>d</sup>				
Favored (%)	98.6		97.2	98.8
Allowed (%)	1.4		2.6	1.2
Outliers (%)	0		0.2	0

Numbers in parentheses represent the value for the highest-resolution shell. Rmsd, root-mean-square deviation.

<sup>a</sup> $R_{\text{merge}} = \sum |I_i - \langle I \rangle| / \sum I_i$ , where  $I_i$  is the intensity of measured reflection and  $\langle I \rangle$  is the mean intensity of all symmetry-related reflections.

<sup>b</sup> $R_{\text{cryst}} = \sum ||F_{\text{calc}}| - |F_{\text{obs}}|| / \sum F_{\text{obs}}$ , where  $F_{\text{obs}}$  and  $F_{\text{calc}}$  are observed and calculated structure factors.

<sup>c</sup> $R_{\text{free}} = \sum_T ||F_{\text{calc}}| - |F_{\text{obs}}|| / \sum F_{\text{obs}}$ , where T is a test dataset of about 5% or 10% of the total unique reflections randomly chosen and set aside prior to refinement.

<sup>d</sup>*B* factors and Ramachandran plot statistics are calculated using MolProbity (Chen et al., 2010).

and Myo6 have SAH prediction scores above a critical threshold (Figure 2C), a result consistent with a previous prediction (Peckham, 2011). We believe that myosins with predicted SAH score below 2.0 do not contain SAH, as the regions predicted to be SAH in these myosins overlap with their coiled-coil regions (e.g., the known coiled-coil dimerization domain of Myo5a). For Myo7a and Myo10, the predicted SAHs partially overlap with or begin directly after the last IQ motif. For Myo6, the predicted SAH partially overlap with the last helix ( $\alpha$ 3) of the three-helix bundle lever arm extension (Mukherjee et al., 2009; Yu et al., 2012) (Figure 2D). Taken together, the structure of the IQ5-SAH/apo-CaM complex and the amino acid sequence analysis discussed above strongly suggest that, in addition to Myo7a, Myo10 also contains a rigid lever arm extending SAH smoothly connected to their respective last IQ motif.

### Myo7a IQ5 Also Binds Ca<sup>2+</sup>-CaM

The generally accepted paradigm of myosin IQ motifs is that IQ motifs can specifically bind to apo-CaM, and a rise in cellular

Ca<sup>2+</sup> concentration leads to dissociation or at least weakened binding of Ca<sup>2+</sup>-CaM. However, there exist examples that certain IQ motifs from myosins can bind to apo-CaM as well as to Ca<sup>2+</sup>-CaM (Lu et al., 2012b, 2015; Zhu et al., 1998). We thus asked whether Myo7a IQ5 may also bind to Ca<sup>2+</sup>-CaM. For the IQ5-SAH and CaM mixture, in buffer containing either EDTA or CaCl<sub>2</sub>, the molar masses of the complex measured by the light-scattering experiments are essentially identical and fit well with a 1:1 stoichiometry (Figure 3A), indicating that one molecule of Ca<sup>2+</sup>-CaM can stably bind to IQ5-SAH. To rule out the possibility that SAH instead of IQ5 might be the Ca<sup>2+</sup>-CaM binding site of IQ5-SAH, we truncated SAH from the IQ5-SAH and tested its binding to CaM. FPLC-SLS showed that IQ5 alone can still form a stable 1:1 complex with CaM in buffers containing either EDTA or CaCl<sub>2</sub> (Figure 3B), indicating that IQ5 can bind to both apo- and Ca<sup>2+</sup>-CaM. The different elution volumes of the IQ5/CaM complexes in the two buffer conditions indicated that the conformations of the complex in the Ca<sup>2+</sup>-free and Ca<sup>2+</sup>-saturated conditions are different.

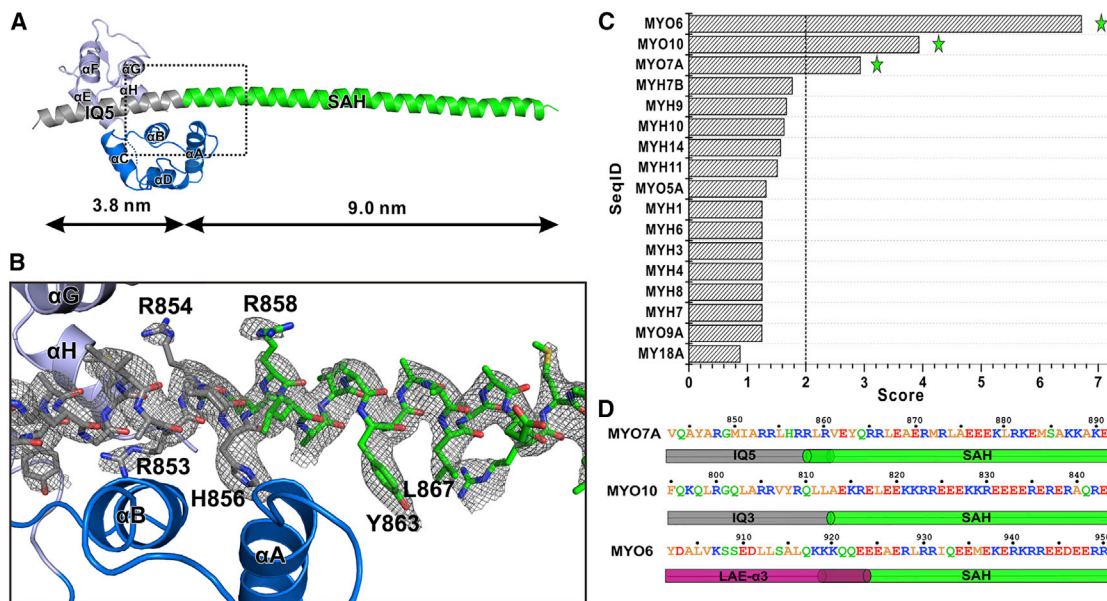


**Figure 2. Structure of Myo7a IQ5-SAH in Complex with apo-CaM**

(A) Ribbon diagram of Myo7a IQ5-SAH in complex with apo-CaM. IQ5 is colored in gray and SAH is in green. The N lobe and C lobe of CaM are colored blue and light blue, respectively. This color-coding scheme is used throughout subsequent figures.

(B) Electron density of the IQ5-SAH junctional region contoured at  $1\sigma$ .

(C) SAHs found by the program scan4csah in all myosins in the mouse proteome (indicated with green stars). The SAHs with score below 2.0 were proved to be coiled coil. The score of 2.0 was chosen as the threshold for SAH, as the predicted SAH with scores below 2.0 are actually part of the coiled coils of myosins. (D) Secondary structure analysis of Myo7a, Myo10, and Myo6 showed continuous helix formation of SAH following the distal IQ motifs (or  $\alpha 3$  of Myo6 LAE). The boundaries of SAHs are based on the predictions by the scan4csah program. The boundaries for the segments preceding SAHs are from the IQ/apo-CaM structures and the structure of Myo6 LAE (PDB: 2LD3).

See also [Figure S1](#).

To understand the structural basis governing the interaction between IQ5 and  $\text{Ca}^{2+}$ -CaM, we determined the crystal structure of Myo7a-IQ5/ $\text{Ca}^{2+}$ -CaM complex at 2.35-Å resolution, using a strategy of co-expressing IQ5 (amino acids 828–870) with  $\text{Ca}^{2+}$ -CaM to obtain a high-quality complex sample (Table 1).  $\text{Ca}^{2+}$ -CaM binds to IQ5 in parallel (i.e., with the N lobe of CaM interacting with the N-terminal half of IQ5 and the C lobe interacting with the C-terminal half of IQ5, Figure 3C, left). In the presence of  $\text{Ca}^{2+}$ , the EF hands in both lobes of CaM adopt a typical open conformation. Phe833 and Leu837 from IQ5 insert into the N-lobe hydrophobic pocket, and Tyr846 and Met850 of IQ5 anchor into the C-lobe hydrophobic pocket of CaM (Figure 3C, left), resulting in a highly compact  $\text{Ca}^{2+}$ -CaM/IQ5 complex structure similar to many well-studied high-affinity  $\text{Ca}^{2+}$ -CaM/target complexes (Hoefflich and Ikura, 2002; Tidow and Nissen, 2013). The solubility of the isolated IQ5 peptide is extremely low, which has prevented us from measuring the quantitative binding constant of the  $\text{Ca}^{2+}$ -CaM/IQ5 complex.

Comparison of the apo-CaM/IQ5-SAH and  $\text{Ca}^{2+}$ -CaM/IQ5 complex structures reveals several important insights. For easy viewing, we have aligned the IQ5 helix from the two structures into the exact same position (Figure 3C). The binding of  $\text{Ca}^{2+}$  to CaM flips the overall orientation of CaM in binding to IQ5. In the apo-CaM/IQ5-SAH complex, the CaM C lobe is anchored by the Val843 of IQ5 (a residue equivalent to the signature Ile residue of the “IQ” motif) and the CaM N lobe weakly engages several residues at the C-terminal half of the IQ motif (Figure 3C,

left), adopting a so-called antiparallel binding mode. Upon  $\text{Ca}^{2+}$  binding, the CaM N lobe moves along the IQ5 helix by  $\sim 4$  nm (or eight helix turns) toward IQ4 and anchors by the two hydrophobic residues (Phe833 and Leu837) at the beginning of IQ5, and the C lobe moves slightly toward C-terminal end of the IQ5 helix by  $\sim 0.5$  nm (or one helix turn), resulting in a parallel and more extended  $\text{Ca}^{2+}$ -CaM/target binding mode (Figure 3C, left). This  $\text{Ca}^{2+}$ -induced CaM binding change leads to the exposure of  $\sim 2.5$  helix turns ( $\sim 9$  residues) located exactly at the junctional region between IQ5 and SAH to solvent (Figure 3C). We also noted that the N lobe of  $\text{Ca}^{2+}$ -CaM covers part of the IQ4 sequence, indicating that the concatenated IQ45 together instead of IQ5 alone serves as the high-affinity  $\text{Ca}^{2+}$ -CaM binding sequence. This phenomenon has also been observed in Myo5a, where pairs of tandemly connected IQ motifs bind to  $\text{Ca}^{2+}$ -CaM with higher affinity than to apo-CaM (Martin and Bayley, 2004).

### **Ca<sup>2+</sup>-Induced Softening of the Myo7a IQ5-SAH Lever Arm Extension**

Our structural analysis has shown that the junctional region between IQ5 and SAH is not protected by CaM when  $\text{Ca}^{2+}$  is present, and this  $\text{Ca}^{2+}$ -induced change in binding mode may affect the conformational flexibility of the IQ5-SAH helix (Figure 4A). To test this hypothesis, we used trypsin partial digestion to probe possible flexibility changes of IQ5-SAH induced by the binding of  $\text{Ca}^{2+}$  to CaM. For digestion performed in the presence of EDTA in the reaction buffer, the IQ5-SAH/CaM complex is stable

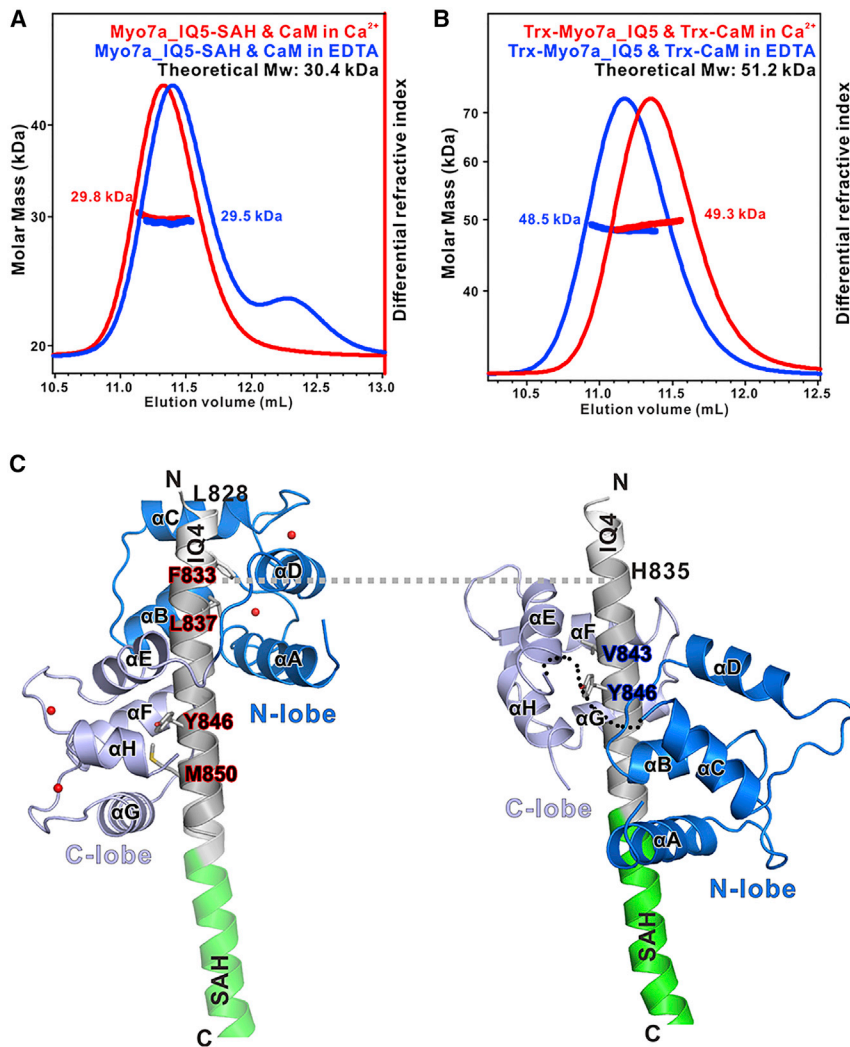


**Figure 3. Biochemical and Structural Analysis of the Myo7a-IQ5/CaM Interaction**

(A) FPLC-SLS showing that Myo7a-IQ5-SAH and CaM form a 1:1 complex both in the presence and absence of  $\text{Ca}^{2+}$ .

(B) FPLC-SLS showing that Trx-tagged Myo7a-IQ5 and Trx-tagged CaM also form a 1:1 complex both in the presence and absence of  $\text{Ca}^{2+}$ .

(C) Ribbon diagram showing the structure of Myo7a-IQ5 in complex with  $\text{Ca}^{2+}$ -CaM (left) or apo-CaM (right). The hydrophobic residues critical for binding are highlighted by the stick model.  $\text{Ca}^{2+}$  ions are shown in red spheres. In this comparison, the IQ5 motifs in the two structures are aligned with the exact same position.

and most of the complex remained intact after 2 hr of digestion at room temperature (Figure 4A). In contrast, in the presence of  $\text{Ca}^{2+}$  in the digestion buffer a significant amount of IQ5-SAH degradation could be observed within the first 5 min of the digestion reaction. Essentially all IQ5-SAH was digested when the reaction reached 1.5 hr (Figure 4A). The trypsin-digested sample mixture in the  $\text{Ca}^{2+}$ -containing buffer was further analyzed by analytical size-exclusion chromatography. An obvious difference can be observed between the digested sample and the undigested control (Figure 4B). We analyzed the trypsin digestion product of the IQ5-SAH/ $\text{Ca}^{2+}$ -CaM mixture by SDS-PAGE and found that the digested product still contains the IQ5/ $\text{Ca}^{2+}$ -CaM complex while the SAH part has been removed from the trypsin digestion (Figures 4C and 4D). The trypsin digestion pattern indicated that the cutting site is likely located within the junctional region between IQ5 and SAH, as this is the only region that undergoes  $\text{Ca}^{2+}$ -dependent exposure to the solvent.

We also used molecular dynamics (MD) simulations to evaluate the  $\text{Ca}^{2+}$ -induced flexibility changes. For both systems, with and without  $\text{Ca}^{2+}$ , five individual 40-ns MD simulations were carried out. Interestingly, in the presence of  $\text{Ca}^{2+}$  we observed that the

junctional region has a clear tendency to unfold (see the population at non-helical region for backbone dihedral angles of residue at junctional region, Leu859, in the simulations of  $\text{Ca}^{2+}$ -CaM-bound IQ5-SAH, Figure S2). For example, in a representative simulation we can see that the junction region began to bend after 14 ns and completely unfold at 20 ns in the presence of  $\text{Ca}^{2+}$  (Figure 4E). In contrast, without  $\text{Ca}^{2+}$  the junction region retained its helical conformational in the first 20 ns (Figure 4E). This structural flexibility induced by the  $\text{Ca}^{2+}$  binding can also be clearly demonstrated by tracing the change of the backbone torsion angle in our MD simulations for the junction residue Leu859. As shown in the Ramachandran plot, the system with  $\text{Ca}^{2+}$  quickly escapes the helical region, indicating the unfolding of the helix (red line in Figure 4F). In contrast, the system without  $\text{Ca}^{2+}$  stays

in the helical region throughout the MD simulation (blue line in Figure 4F). As a control, we also show that residues not located in the junctional region (e.g., Arg848 on IQ5 and Arg881 on SAH) remain in the helical conformation in both systems (Figure 4F), suggesting that the structural changes induced by the  $\text{Ca}^{2+}$  binding are concentrated in the junctional region.

We have also compared CD-based thermal denaturation profiles of the  $\text{Ca}^{2+}$ -CaM/IQ5-SAH complex and the apo-CaM/IQ5-SAH complex. Interestingly, the  $\text{Ca}^{2+}$ -CaM bound complex is less stable than the apo-CaM bound IQ5-SAH complex (Figure S3). It is well known that  $\text{Ca}^{2+}$ -CaM is much more resistant to thermal denaturation than apo-CaM (Brzeska et al., 1983). The lower overall stability of  $\text{Ca}^{2+}$ -CaM/IQ5-SAH complex with respect to the apo-CaM/IQ5-SAH complex is likely the result of the decreased stability of the IQ5 and SAH junctional region upon  $\text{Ca}^{2+}$  binding, as the IQ5 region and the SAH region are the same in both complexes. Taken together, we propose that binding of  $\text{Ca}^{2+}$  to CaM can increase the conformational flexibility of the IQ5-SAH lever arm extension of Myo7a and thereby may regulate mechanical force transduction of the motor.

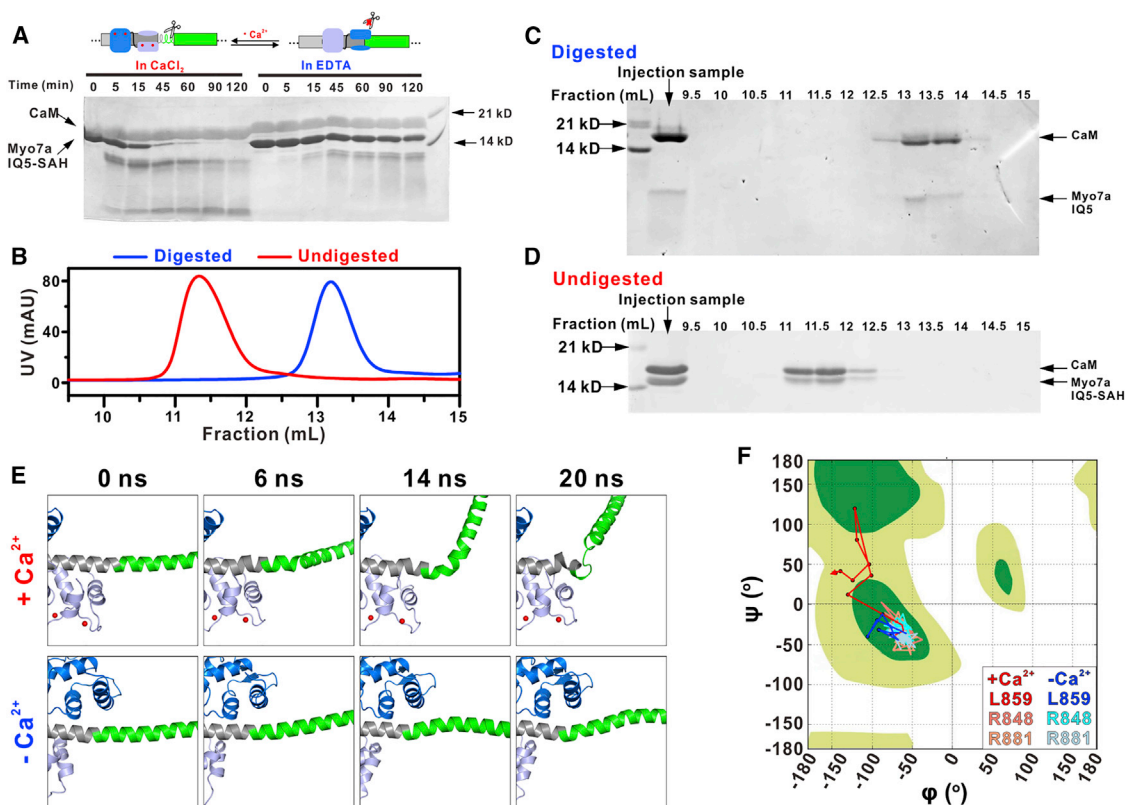


**Figure 4.  $\text{Ca}^{2+}$ -Induced Flexibility Change of the Myo7a IQ5-SAH/CaM Complex**

(A) Trypsin partial digestions of the Myo7a-IQ5-SAH/CaM complex in the EDTA or  $\text{CaCl}_2$  buffer. Difference in digestion pattern indicates that  $\text{Ca}^{2+}$  plays a role in regulating the continuity and rigidity of the IQ5-SAH helix, as illustrated by the scheme above the figure.

(B) Analytical gel filtration chromatography profiles of the trypsin-digested (blue line) and undigested control (red line) samples of the Myo7a-IQ5-SAH/CaM complex in  $\text{CaCl}_2$  buffer.

(C and D) SDS-PAGE analysis of the corresponding fractions from chromatography results in (B).

(E) Snapshots at different time points during the simulations in the presence (upper) or absence (lower) of  $\text{Ca}^{2+}$  showing the conformational changes of junctional region.

(F) Backbone dihedral angle trajectories of Arg848, Arg881, and Leu859 in the Ramachandran plots in the presence (red lines for Leu859, light-red line for Arg848 and Arg881) or absence (blue lines for Leu859, light-blue line for Arg848 and Arg881) of  $\text{Ca}^{2+}$ . Green areas represent the favored regions and the shallow green areas represent the allowed regions.

See also [Figures S2](#) and [S3](#).

### **IQ Motifs in Other Myosins Can Also Bind to $\text{Ca}^{2+}$ -CaM**

Detailed biochemical and structural analyses have already shown that Myo7a-IQ5 can bind to both apo- and  $\text{Ca}^{2+}$ -CaM. Given our previous finding that Myo1c-IQ3 also binds to both apo- and  $\text{Ca}^{2+}$ -CaM ([Lu et al., 2015](#)), we wondered whether IQ motifs in other unconventional myosins may behave similarly. Considering that both Myo7a-IQ5 and Myo1c-IQ3 are located at the distal ends of the lever arms, we focused on the last IQ motifs in several unconventional myosins and characterized their interactions with apo- and  $\text{Ca}^{2+}$ -CaM using isothermal titration calorimetry (ITC)-based experiments. Another reason for picking the last IQ motif for study is that it represents the connecting point between the lever arm and the tail cargo binding domain of each myosin. We first tested IQ3 in Myo10, because both Myo10 and Myo7a are MyTH4-FERM-containing myosins and both have SAHs following the last IQ motifs. The ITC experiments showed that the Myo10 IQ3 peptide can bind to both apo- and  $\text{Ca}^{2+}$ -CaM. The affinity of IQ3 to apo-CaM was moderate, with

a  $K_D$  of 6.5  $\mu\text{M}$ . However, in the presence of  $\text{Ca}^{2+}$  the affinity is about 30-fold stronger ( $K_D \sim 0.21 \mu\text{M}$ , [Figure 5A](#)). Similarly, the last IQ of Myosin IXa (Myo9a-IQ6) and the last IQ of Myosin XVa (Myo15a-IQ3) both bind to  $\text{Ca}^{2+}$ -CaM considerably stronger than to apo-CaM ([Figures 5B](#) and [S4](#)). We have also tried to test a few more distal IQ motifs from other myosins. The low solubility of Myo5a-IQ6 peptide prevented us from deriving any binding data. Myosin IIIa-IQ2 had very weak apo-CaM binding ( $K_D$  of dozens of  $\mu\text{M}$ ) and essentially no  $\text{Ca}^{2+}$ -CaM binding (data not shown).

The structure of Myo7a IQ5/ $\text{Ca}^{2+}$ -CaM complex shows that residues at the positions “-10,” “-6,” “3,” and “7” are the four anchoring points for  $\text{Ca}^{2+}$ -CaM recognition (the Ile in the signature “IQ” sequence in each IQ motif is defined as the position “0,” see [Figure 5C](#)). There are also two different  $\text{Ca}^{2+}$ -CaM recognition modes in non-myosin IQ motifs. One is found in voltage-gated calcium channels and a protein called IQ motif containing G ([Chen et al., 2014](#); [Kim et al., 2008](#); [Mori et al.,](#)

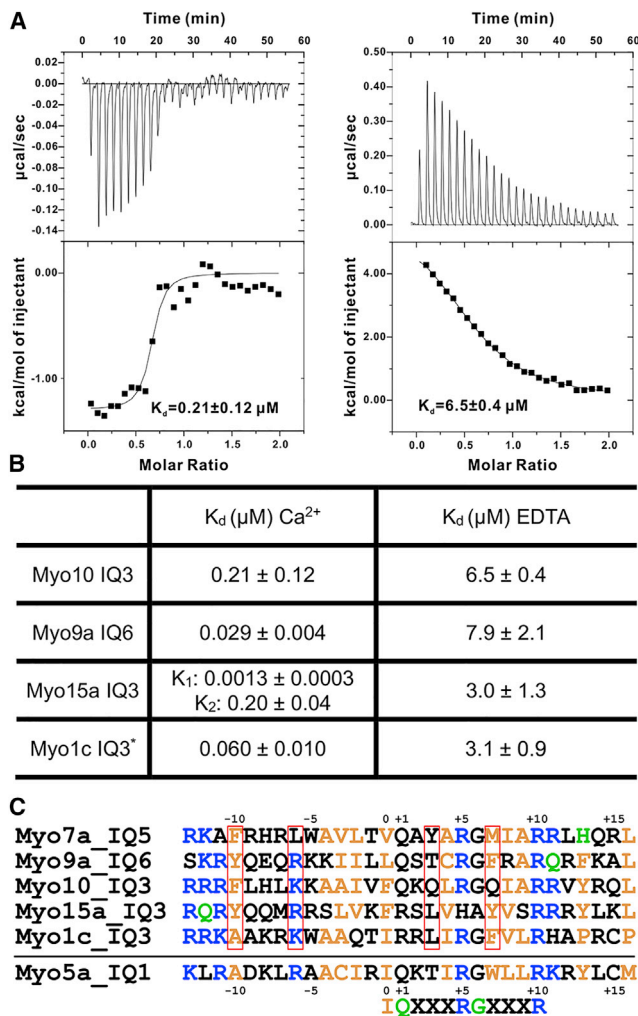


**Figure 5. IQ Motifs from Other Myosins Can Bind to Both apo- and  $\text{Ca}^{2+}$ -CaM**

(A) ITC titration curves showing the binding affinities of  $\text{Ca}^{2+}$ -CaM (left) and apo-CaM (right) to the Myo10-IQ3 peptide.

(B) Summary of the ITC-derived binding results of several distal IQ motifs of myosins tested in this study. Myo10-IQ3, Myo9a-IQ6, and Myo15a-IQ3, together with the previously reported Myo1c-IQ3, can bind to both apo- and  $\text{Ca}^{2+}$ -CaM. In all these cases,  $\text{Ca}^{2+}$ -CaM binds to these IQ motifs with higher affinities than does apo-CaM.

(C) Sequence alignment of the IQ motifs that can interact with both apo- and  $\text{Ca}^{2+}$ -CaM tested in this study. The red box highlights the positions of the residues critical for anchoring Myo7a-IQ5 to  $\text{Ca}^{2+}$ -CaM. The Myo5a-IQ1 sequence and the IQ consensus sequence are included for reference. See also Figure S4.

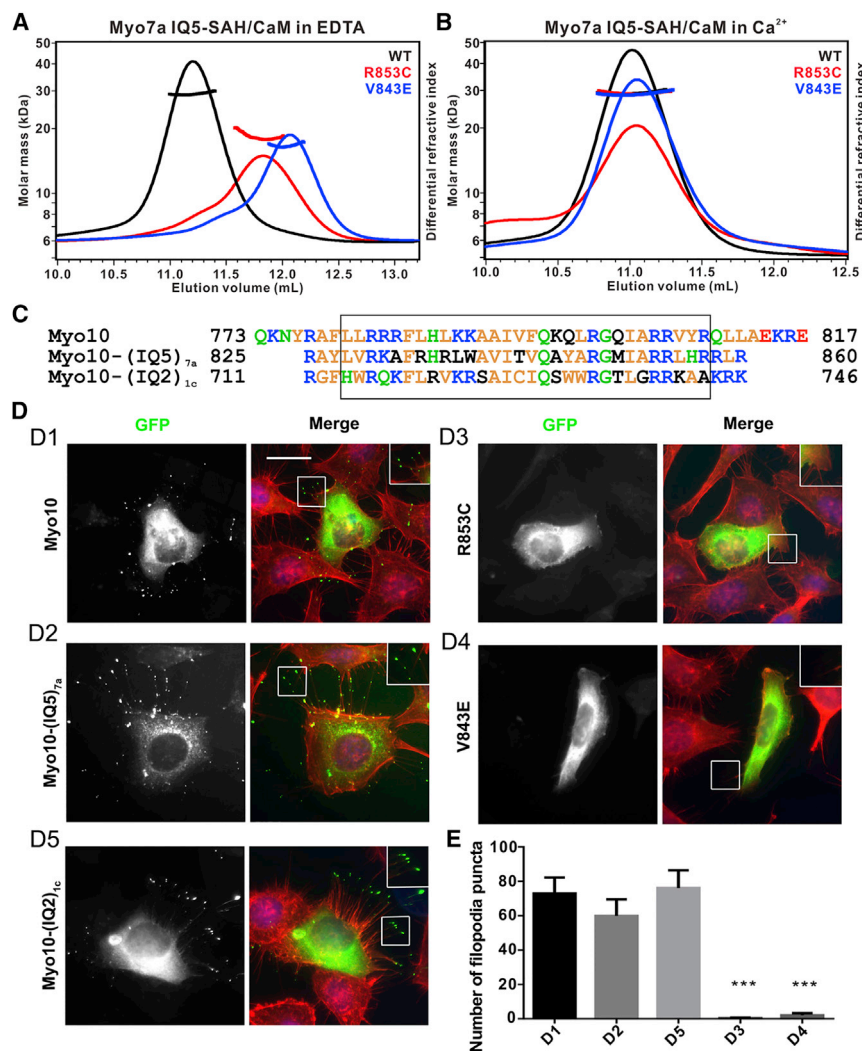
2008; Van Petegem et al., 2005), in which residues at the positions “-6” and “3” are responsible for anchoring to CaM. Another binding mode is found in voltage-gated sodium channels (Wang et al., 2014), in which residues at the positions “0” and “9” are two anchoring points for CaM. Alignment of the  $\text{Ca}^{2+}$ -CaM binding IQ motifs from myosins characterized in this study shows that except for Myo1c-IQ3, the other three IQ motifs listed in Figure 5B cannot be fitted into any of the known  $\text{Ca}^{2+}$ -CaM/IQ binding patterns (Figure 5C), illustrating the remarkable capacity of CaM to bind to diverse target proteins

(Hoeflich and Ikura, 2002; Tidow and Nissen, 2013). The exact binding modes of these myosin IQ motifs will need further structural characterization.

### The R853C Mutation of Myo7a Found in DFNA11 Is Functionally Defective Due to Its Loss of Apo-CaM Binding

Human genetic studies have identified a single-point missense mutation, R853C, in Myo7a IQ5, which can cause autosomal dominant hearing loss DFNA11 (Bolz et al., 2004). The structure of the IQ5/apo-CaM complex shows that Arg853, which is located at position “10” of the IQ motif, forms several hydrogen bonds with both backbone and side chain of residues from both lobes of apo-CaM (Figure S5A). Mutation of this residue to a small and uncharged Cys will disrupt these hydrogen bonds, thus decreasing the binding affinity between IQ5 and apo-CaM. However, in the structure of IQ5/ $\text{Ca}^{2+}$ -CaM complex, the side chain of Arg853 is exposed to solvent and electron density is missing, indicating that this Arg is not involved in the interaction with  $\text{Ca}^{2+}$ -CaM (Figure S5B). We used FPLC-SLS to evaluate the effect of the mutation. Consistent with our analysis, essentially no IQ5/apo-CaM complex peak was observed when mixing R853C-IQ5-SAH with apo-CaM (Figure 6A). In contrast, in buffer containing  $\text{CaCl}_2$ , both the elution profile and the fitted molar mass of the mutant IQ5-SAH/ $\text{Ca}^{2+}$ -CaM complex are almost identical to those of the wild-type IQ5-SAH/ $\text{Ca}^{2+}$ -CaM complex (Figure 6B). Based on the structures of Myo7a IQ5 bound to apo- and  $\text{Ca}^{2+}$ -CaM, Val843 in the “0” position of the IQ motif is critical for its binding to apo-CaM, but this residue is not in contact with  $\text{Ca}^{2+}$ -CaM (Figure 3C). Therefore, substitution of Val843 with Glu is expected to eliminate the IQ5’s binding to apo-CaM but has no impact on  $\text{Ca}^{2+}$ -CaM binding. Indeed, FPLC-SLS analysis showed that V843E-IQ5-SAH has no detectable binding to apo-CaM, and the mutant behaves the same as the wild-type counterpart in binding to  $\text{Ca}^{2+}$ -CaM (Figures 6A and 6B). This analysis suggests that the DFNA11 missense mutation specifically affects the apo-CaM binding but not the  $\text{Ca}^{2+}$ -CaM binding of Myo7a.

Next, we tried to set up a cell-based assay to evaluate the impact of the DFNA11 missense mutation. It has been reported that when forced into a dimer, Myo7a can target to the tips of filopodia when overexpressed in heterologous cells (Sakai et al., 2011, 2015). However, in our hands neither the full-length wild-type Myo7a nor the motor-SAH construct fused to a GCN4 dimer can localize to the tip of filopodia in HeLa cells. Another MyTH4-FERM-containing myosin (Myo10), when overexpressed, can robustly induce filopodia formation as well as target the motor to the tips of filopodia (Kerber and Cheney, 2011; Lu et al., 2012a). We used a chimera strategy by replacing Myo10-IQ3 with Myo7a-IQ5 to evaluate the structural/functional relationship of Myo7-IQ5, as both IQ motifs can bind to apo- and  $\text{Ca}^{2+}$ -CaM as well as form a continuous helix with the immediately following SAH. The position selected for the IQ motif swap is carefully designed and based on the structure shown in Figure 3 and the amino acid sequence alignment of the IQ motifs (Figure 6C). As expected, when overexpressed in HeLa cells, the GFP-tagged full-length Myo10 are enriched at the tips of numerous elongated filopodia (Figure 6D1). By replacing its IQ3 with Myo7a IQ5 (denoted as Myo10-(IQ5)<sub>7a</sub>, Figure 6C), the filopodia tip localization



of the chimera Myo10 is essentially the same as that of the wild-type motor (Figures 6D2 and 6E). In total contrast, the Myo10 chimera with its IQ3 replaced by the Myo7a R853C-IQ5 showed essentially no elongated filopodia and no filopodia tip localization (Figures 6D3 and 6E), indicating that the R853C mutation causing loss of apo-CaM binding compromised the function of chimera Myo10. Using the same chimera strategy, we further demonstrated that loss of apo-CaM binding caused by the V843E mutation of Myo7a-IQ5 also eliminated filopodia induction capacity of the chimera Myo10 (Figures 6D4 and 6E). Since processive walking on bundled actin filaments is essential for the filopodia induction and tip localization of Myo10 (Lu et al., 2012a), the failed filopodia induction and tip localization of the two Myo10 chimeras bearing the Myo7a IQ5 mutants are presumably caused by loss of the lever arm rigidity of the mutant chimeras. We also wanted to test the role of Ca<sup>2+</sup>-CaM binding to IQ5 using the same chimera approach. However, this effort was not successful, as we were unable to find a single-point mutation either in Myo7a IQ5 or Myo10 IQ3 that can specifically disrupt their Ca<sup>2+</sup>-CaM binding but retain the apo-CaM binding. As an alternative, we designed another chimera by replacing

### Figure 6. Biochemical and Functional Effect of the R853C DFNA11 Mutation of Myo7a

(A and B) FPLC-SLS results showing that the R853C mutation and the V843E mutation affect their respective Myo7a-IQ5/apo-CaM binding (A) but not their Myo7a-IQ5/Ca<sup>2+</sup>-CaM binding (B). (C) The design of the Myo10 chimera constructs. The black box highlights the sequences of Myo7a-IQ5 and Myo1c-IQ2 used to replace Myo10-IQ3. (D) Representative images of HeLa cells transfected with various GFP-tagged constructs and with actin filament stained with phalloidin (red), and nuclei stained with DAPI (blue): D1, Myo10; D2, Myo10-(IQ5)<sub>7a</sub>; D3, Myo10-R853C-(IQ5)<sub>7a</sub>; D4, Myo10-V843E-(IQ5)<sub>7a</sub>; D5, Myo10-(IQ2)<sub>1c</sub>. Scale bar, 20 μm. (E) Quantitative analysis of GFP puncta number per cell at the tips of filopodia. Values are means ± SD from three independent experiments with >10 cells per experiment, using an unpaired t test. \*\*\*p < 0.001. See also Figure S5.

Myo10-IQ3 with Myo1c-IQ2 (denoted Myo10-(IQ2)<sub>1c</sub>, Figure 6C), which we have previously shown to interact only with apo-CaM but not with Ca<sup>2+</sup>-CaM (Lu et al., 2015). The Myo10 chimera carrying the Myo1c IQ2 can induce filopodia elongation and target to the tips of filopodia as well as the wild-type motor (Figures 6D5 and 6E).

## DISCUSSION

### Possible Roles of SAH in the Function of Myo7a

The crystal structure of Myo7a-IQ5-SAH/apo-CaM complex provided direct structural evidence supporting the view that an SAH following a distal IQ motif can indeed function as a lever arm extension of a myosin motor. Myo7a contains five IQ motifs forming the canonical lever arm with a length of ~19 nm. The SAH further extends the lever arm length by ~9 nm, thereby granting Myo7a the longest lever arm among all vertebrate unconventional myosins. The exact cellular function of having such a long lever arm for Myo7a will require further study, as whether the motor functions as a cargo transporter or mechanical tether (or both) is still not clear. Intuitively, the SAH-mediated extension of the rigid lever arm may allow monomeric Myo7a to tether motor head-attached actin filaments with tail-bound membrane cargoes with a wider space and to transduce mechanical force between a motor head and cargo binding tail. If Myo7a, analogous to Myo6, forms a cargo binding-induced dimer (Sakai et al., 2011; Yu et al., 2009), the dimerized motor with an extended lever arm containing rigid SAH may increase the step size of the motor on actin filaments. Importantly, the conformational rigidity of the Myo7a lever arm extension can be regulated by cellular Ca<sup>2+</sup> concentration changes. Increasing the cellular Ca<sup>2+</sup> concentration softens the rigidity of the Myo7a lever arm extension.

### Possible Roles of IQ/Ca<sup>2+</sup>-CaM Binding

In Myo7a, the Ca<sup>2+</sup>-induced CaM binding mode change can cause a breakage/softening of the continuous helix formed between IQ5 and SAH. This will lead to the loss of rigidity in the lever arm, meaning that the motor cannot function properly in the presence of Ca<sup>2+</sup>. However, this mechanism does not explain why Ca<sup>2+</sup>-CaM needs to remain associated with the IQ motif with an even higher affinity. One could argue that a simple Ca<sup>2+</sup>-induced dissociation of CaM can achieve the same lever arm-softening effect. Additionally we showed that high-affinity binding of Ca<sup>2+</sup>-CaM to the most distal IQ motif seems to be a rather common property for a number of myosins. It is possible that retained Ca<sup>2+</sup>-CaM binding to IQ motifs may maintain the lever arm to be partially structured even when myosins are in their off-state upon elevation of Ca<sup>2+</sup> concentration. When cells return to their resting state, formation of the rigid lever arms of myosins does not require a complete refolding process, thereby shortening the recovery time required for motors to return to their working state. Second, the retained binding of Ca<sup>2+</sup>-CaM to IQ motifs provides a mechanism for CaM to be a continuous resident protein of myosins. With such a CaM molecule residing at an IQ motif, this IQ motif can rapidly bind to the same CaM when cellular concentration drops, as otherwise the binding has to wait for diffusion-mediated encounter of another CaM molecule in cytosol. Such resident CaM on IQ motifs may significantly speed up the functional recovery of myosins in response to changes in cellular Ca<sup>2+</sup> concentration. Similar resident CaM-facilitated rapid IQ motif rebinding by apo-CaM has been demonstrated to be critical for kinetics of Ca<sup>2+</sup>-dependent activations of Ca<sup>2+</sup> and Na<sup>+</sup> channels (Ben-Johny and Yue, 2014; DeMaria et al., 2001).

Recently, it was shown that CaM in Myo6 can also undergo a Ca<sup>2+</sup>-induced binding rearrangement in the motor's lever arm region (Batters et al., 2016). Combined with low-resolution electron microscopy-based study, the authors proposed a model describing Ca<sup>2+</sup>-mediated regulation of Myo6 activity (Batters et al., 2016). In this model, Myo6 adopts a tail-backfolded, auto-inhibited conformation at low Ca<sup>2+</sup> concentration state. Upon rise of Ca<sup>2+</sup> concentration, Ca<sup>2+</sup>-induced CaM binding rearrangement leads to release of Myo6's auto-inhibition and converts the motor into a non-motile but primed state capable of cargo binding. Interestingly, binding of Ca<sup>2+</sup>-CaM to the distal IQ motif of Myo6 also appears to increase the conformational flexibility of the motor lever arm, with the motor thus adopting a non-motile state (Batters et al., 2016). The cargo-loaded motor will further convert into the active, apo-CaM binding state when Ca<sup>2+</sup> concentration returns to low level. A similar mechanism may also apply to Myo7a (Batters and Veigel, 2016). Myo7a also adopts an auto-inhibited conformation in its apo-CaM bound, cargo-free form (Umeki et al., 2009; Yang et al., 2009). Myo7a can undergo Ca<sup>2+</sup>-induced CaM binding rearrangement, as shown in the current study. Finally, cargo binding to the tail of Myo7a can convert the motor into a processive dimer (Sakai et al., 2011).

Our studies on chimeric Myo10 in filopodia inductions in heterologous cells provided a convenient assay for us to investigate roles of apo-CaM binding to Myo7a's IQ motifs in the motor's cellular function. However, it should be pointed out that as this chimera approach is indirect in nature, the derived conclusion

should be viewed as tentative. Further studies will be required to address this question. For example, *in vitro* single-molecule-based assays can be used to assess the impact of Ca<sup>2+</sup> on Myo7a's stepping velocity or stride size and processivity on actin filaments. Alternatively, one might compare functional changes of photoreceptors or hair cells containing the wild-type Myo7a or its CaM binding mutants to obtain more direct evidence pertaining to the roles of apo-CaM and Ca<sup>2+</sup>-CaM on the motor's physiological functions.

### Potential Uses of SAH as a Research Tool

Although the prevalent existence of SAH has been recognized for years, the only structural information is the recently reported crystal structure of Myo10-SAH-antiCC at 3.5-Å resolution (Ropars et al., 2016). However, the low resolution in that study did not allow confident resolution of the side chains and thus cannot provide any details of the structural determinants of the SAH. The crystal structure of Myo7a SAH presented in the current study provides the high-resolution atomic picture of how an isolated, stable SAH is formed. The inter-turn charge-charge interactions contribute to the high stability of the SAH. Given the extremely simple interaction mode observed in the Myo7a SAH structure, it will be feasible to design SAHs with different lengths. With their composition of alternative E and K/R, SAHs are biologically inert, genetically encodable, and length programmable. These unique features, together with their high stability and conformational rigidity, make SAHs attractive molecular rulers to physically position two biomolecules with precise distances (Sivaramakrishnan and Spudich, 2011; Swanson and Sivaramakrishnan, 2014). In addition, a combined use of IQ motifs together with SAH (e.g., based on the Myo7a-IQ5-SAH segment demonstrated in this study) not only can provide genetically encodable spacers for precisely positioning two proteins apart but also allows such spacers (or, more precisely, the conformational flexibility of the spaces) to be regulated by Ca<sup>2+</sup>.

In the construct used for crystallization (residues 866–935), around 60% of the residues are charged residues E/R/K. To the best of our knowledge, Myo7a-866-935 is the protein with the highest percentage of charged residues that has ever been crystallized. To our surprise, this highly charged protein is extremely easy to crystallize. In our initial crystallization screen experiments, many conditions containing polyethylene glycol (PEG) and low concentration of salts yielded high-diffraction-quality crystals. The crystallization of Myo7a SAH is facilitated by the packing of a small stretch of hydrophobic residues (Leu880/Met884 and Leu925/Leu926/Met929). Since it is biologically inert and very easy to crystallize, Myo7a-SAH or its derivatives might be used as a protein crystallization tag for proteins that are difficult to crystallize.

### STAR★METHODS

Detailed methods are provided in the online version of this paper and include the following:

- KEY RESOURCES TABLE
- CONTACT FOR REAGENT AND RESOURCE SHARING
- EXPERIMENTAL MODEL AND SUBJECT DETAILS
  - HeLa Cells Culture

- **METHOD DETAILS**
  - Protein Expression and Purification
  - Static Light Scattering Analysis
  - Circular Dichroism Spectroscopy
  - NMR Spectroscopy
  - Crystallography
  - Sequence Analysis
  - Trypsin Partial Digestion Studies
  - Molecular Dynamics Simulations
  - Isothermal Titration Calorimetry Assay
  - Cellular Localization and Filopodia Quantification
- **QUANTIFICATION AND STATISTICAL ANALYSIS**
- **DATA AND SOFTWARE AVAILABILITY**

### SUPPLEMENTAL INFORMATION

Supplemental Information includes five figures and can be found with this article online at <http://dx.doi.org/10.1016/j.str.2017.02.002>.

### AUTHOR CONTRIBUTIONS

Conceptualization, J.L., Q.L., and M.Z.; Methodology, J.L., Q.L., Y.C., and I.C.U.; Investigation, J.L., Y.C., Y.D., and I.C.U.; Writing – Original Draft, J.L. and M.Z.; Writing – Review & Editing, J.L., Y.C., Y.D., I.C.U., Q.L., X.H., and M.Z.; Funding Acquisition, Q.L., X.H., and M.Z.; Supervision and Coordination, M.Z.

### ACKNOWLEDGMENTS

We thank the Shanghai Synchrotron Radiation Facility (SSRF) BL19U1 and BL17U1 for X-ray beam time and Dr. Quan Hao for accessing the in-house X-ray diffraction machine. This work was supported by grants from RGC of Hong Kong (664113, 16103614, AoE-M09-12, and T13-607/12R), and a 973 program grant from the Minister of Science and Technology of China (2014CB910204) to M.Z.; a grant from RGC of Hong Kong (16149516) to Q.L.; and a grant from RGC of Hong Kong (C6009-15G) to X.H. and M.Z.. M.Z. is a Kerry Holdings Professor in Science and a Senior Fellow of IAS at HKUST.

Received: September 14, 2016

Revised: December 8, 2016

Accepted: February 9, 2017

Published: March 2, 2017

### REFERENCES

- Adams, P.D., Afonine, P.V., Bunkoczi, G., Chen, V.B., Davis, I.W., Echols, N., Headd, J.J., Hung, L.W., Kapral, G.J., Grosse-Kunstleve, R.W., et al. (2010). PHENIX: a comprehensive Python-based system for macromolecular structure solution. *Acta Crystallogr. D Biol. Crystallogr.* **66**, 213–221.
- Baboolal, T.G., Sakamoto, T., Forgacs, E., White, H.D., Jackson, S.M., Takagi, Y., Farrow, R.E., Molloy, J.E., Knight, P.J., Sellers, J.R., et al. (2009). The SAH domain extends the functional length of the myosin lever. *Proc. Natl. Acad. Sci. USA* **106**, 22193–22198.
- Bahler, M., and Rhoads, A. (2002). Calmodulin signaling via the IQ motif. *FEBS Lett.* **513**, 107–113.
- Batters, C., and Veigel, C. (2016). Mechanics and activation of unconventional myosins. *Traffic* **17**, 860–871.
- Batters, C., Brack, D., Ellrich, H., Averbeck, B., and Veigel, C. (2016). Calcium can mobilize and activate myosin-VI. *Proc. Natl. Acad. Sci. USA* **113**, E1162–E1169.
- Ben-Johny, M., and Yue, D.T. (2014). Calmodulin regulation (calmodulation) of voltage-gated calcium channels. *J. Gen. Physiol.* **143**, 679–692.
- Bolz, H., Bolz, S.S., Schade, G., Kothe, C., Mohrmann, G., Hess, M., and Gal, A. (2004). Impaired calmodulin binding of myosin-7A causes autosomal dominant hearing loss (DFNA11). *Hum. Mutat.* **24**, 274–275.
- Brzeska, H., Venyaminov, S.Vu., Grabarek, Z., and Drabikowski, W. (1983). Comparative studies on thermostability of calmodulin, skeletal muscle troponin C and their tryptic fragments. *FEBS Lett.* **153**, 169–173.
- Bussi, G., Donadio, D., and Parrinello, M. (2007). Canonical sampling through velocity rescaling. *J. Chem. Phys.* **126**, 014101.
- Chen, Z.Y., Hasson, T., Zhang, D.S., Schwender, B.J., Derfler, B.H., Mooseker, M.S., and Corey, D.P. (2001). Myosin-VIb, a novel unconventional myosin, is a constituent of microvilli in transporting epithelia. *Genomics* **72**, 285–296.
- Chen, V.B., Arendall, W.B., 3rd, Headd, J.J., Keedy, D.A., Immormino, R.M., Kapral, G.J., Murray, L.W., Richardson, J.S., and Richardson, D.C. (2010). MolProbity: all-atom structure validation for macromolecular crystallography. *Acta Crystallogr. D Biol. Crystallogr.* **66**, 12–21.
- Chen, L.T., Liang, W.X., Chen, S., Li, R.K., Tan, J.L., Xu, P.F., Luo, L.F., Wang, L., Yu, S.H., Meng, G., et al. (2014). Functional and molecular features of the calmodulin-interacting protein IQCG required for haematopoiesis in zebrafish. *Nat. Commun.* **5**, 3811.
- Cheney, R.E., and Mooseker, M.S. (1992). Unconventional myosins. *Curr. Opin. Cell Biol.* **4**, 27–35.
- Cowtan, K. (2006). The Buccaneer software for automated model building. 1. Tracing protein chains. *Acta Crystallogr. D Biol. Crystallogr.* **62**, 1002–1011.
- Crawley, S.W., Shifrin, D.A., Jr., Grega-Larson, N.E., McConnell, R.E., Benesh, A.E., Mao, S., Zheng, Y., Zheng, Q.Y., Nam, K.T., Millis, B.A., et al. (2014). Intestinal brush border assembly driven by protocadherin-based intermicrovillar adhesion. *Cell* **157**, 433–446.
- Crawley, S.W., Weck, M.L., Grega-Larson, N.E., Shifrin, D.A., Jr., and Tyska, M.J. (2016). ANKS4B is essential for intermicrovillar adhesion complex formation. *Dev. Cell* **36**, 190–200.
- Darden, T., York, D., and Pedersen, L. (1993). Particle Mesh Ewald - an N.Log(N) method for ewald sums in large systems. *J. Chem. Phys.* **98**, 10089–10092.
- DeMaria, C.D., Soong, T.W., Alseikhan, B.A., Alvania, R.S., and Yue, D.T. (2001). Calmodulin bifurcates the local Ca<sup>2+</sup> signal that modulates P/Q-type Ca<sup>2+</sup> channels. *Nature* **411**, 484–489.
- Emsley, P., Lohkamp, B., Scott, W.G., and Cowtan, K. (2010). Features and development of Coot. *Acta Crystallogr. D Biol. Crystallogr.* **66**, 486–501.
- Gaspari, Z., Suveges, D., Perczel, A., Nyitrai, L., and Toth, G. (2012). Charged single alpha-helices in proteomes revealed by a consensus prediction approach. *Biochim. Biophys. Acta* **1824**, 637–646.
- Gibson, F., Walsh, J., Mburu, P., Varela, A., Brown, K.A., Antonio, M., Beisel, K.W., Steel, K.P., and Brown, S.D.M. (1995). A type-VII myosin encoded by the mouse deafness gene shaker-1. *Nature* **374**, 62–64.
- Gillespie, P.G., and Muller, U. (2009). Mechanotransduction by hair cells: models, molecules, and mechanisms. *Cell* **139**, 33–44.
- Hartman, M.A., Finan, D., Sivaramakrishnan, S., and Spudich, J.A. (2011). Principles of unconventional myosin function and targeting. *Annu. Rev. Cell Dev. Biol.* **27**, 133–155.
- Heissler, S.M., and Sellers, J.R. (2014). Myosin light chains: teaching old dogs new tricks. *Bioarchitecture* **4**, 169–188.
- Henn, A., and De La Cruz, E.M. (2005). Vertebrate myosin VIIb is a high duty ratio motor adapted for generating and maintaining tension. *J. Biol. Chem.* **280**, 39665–39676.
- Hess, B., Bekker, H., Berendsen, H.J.C., and Fraaije, J.G.E.M. (1997). LINC: a linear constraint solver for molecular simulations. *J. Comput. Chem.* **18**, 1463–1472.
- Hoeflich, K.P., and Ikura, M. (2002). Calmodulin in action: diversity in target recognition and activation mechanisms. *Cell* **108**, 739–742.
- Houdusse, A., Gaucher, J.F., Krementsova, E., Mui, S., Trybus, K.M., and Cohen, C. (2006). Crystal structure of apo-calmodulin bound to the first two IQ motifs of myosin V reveals essential recognition features. *Proc. Natl. Acad. Sci. USA* **103**, 19326–19331.

- Jorgensen, W.L., and Madura, J.D. (1983). Quantum and statistical studies of liquids. 25. Solvation and conformation of methanol in water. *J. Am. Chem. Soc.* *105*, 1407–1413.
- Kerber, M.L., and Cheney, R.E. (2011). Myosin-X: a MyTH-FERM myosin at the tips of filopodia. *J. Cell Sci.* *124*, 3733–3741.
- Kim, E.Y., Rumpf, C.H., Fujiwara, Y., Cooley, E.S., Van Petegem, F., and Minor, D.L., Jr. (2008). Structures of CaV2 Ca<sup>2+</sup>/CaM-IQ domain complexes reveal binding modes that underlie calcium-dependent inactivation and facilitation. *Structure* *16*, 1455–1467.
- Knight, P.J., Thirumurugan, K., Xu, Y.H., Wang, F., Kalverda, A.P., Stafford, W.F., Sellers, J.R., and Peckham, M. (2005). The predicted coiled-coil domain of myosin 10 forms a novel elongated domain that lengthens the head. *J. Biol. Chem.* *280*, 34702–34708.
- Lefevre, G., Michel, V., Weil, D., Lepelletier, L., Bizard, E., Wolfrum, U., Hardein, J.P., and Petit, C. (2008). A core cochlear phenotype in USH1 mouse mutants implicates fibrous links of the hair bundle in its cohesion, orientation and differential growth. *Development* *135*, 1427–1437.
- Li, J., He, Y., Lu, Q., and Zhang, M. (2016). Mechanistic basis of organization of the harmonin/USH1C-mediated brush border microvilli tip-link complex. *Dev. Cell* *36*, 179–189.
- Lindorff-Larsen, K., Piana, S., Palmo, K., Maragakis, P., Klepeis, J.L., Dror, R.O., and Shaw, D.E. (2010). Improved side-chain torsion potentials for the Amber ff99SB protein force field. *Proteins* *78*, 1950–1958.
- Liu, X., Ondek, B., and Williams, D.S. (1998). Mutant myosin VIIa causes defective melanosome distribution in the RPE of shaker-1 mice. *Nat. Genet.* *19*, 117–118.
- Liu, X., Vansant, G., Udovichenko, I.P., Wolfrum, U., and Williams, D.S. (1997a). Myosin VIIa, the product of the Usher 1B syndrome gene, is concentrated in the connecting cilia of photoreceptor cells. *Cell Motil. Cytoskeleton* *37*, 240–252.
- Liu, X.Z., Walsh, J., Mburu, P., Kendrick-Jones, J., Cope, M.J., Steel, K.P., and Brown, S.D.M. (1997b). Mutations in the myosin VIIa gene cause non-syndromic recessive deafness. *Nat. Genet.* *16*, 188–190.
- Liu, X.Z., Walsh, J., Tamagawa, Y., Kitamura, K., Nishizawa, M., Steel, K.P., and Brown, S.D. (1997c). Autosomal dominant non-syndromic deafness caused by a mutation in the myosin VIIa gene. *Nat. Genet.* *17*, 268–269.
- Lu, Q., Ye, F., Wei, Z.Y., Wen, Z., and Zhang, M.J. (2012a). Antiparallel coiled-coil-mediated dimerization of myosin X. *Proc. Natl. Acad. Sci. USA* *109*, 17388–17393.
- Lu, Z., Shen, M., Cao, Y., Zhang, H.M., Yao, L.L., and Li, X.D. (2012b). Calmodulin bound to the first IQ motif is responsible for calcium-dependent regulation of myosin 5a. *J. Biol. Chem.* *287*, 16530–16540.
- Lu, Q., Li, J., Ye, F., and Zhang, M. (2015). Structure of myosin-1c tail bound to calmodulin provides insights into calcium-mediated conformational coupling. *Nat. Struct. Mol. Biol.* *22*, 81–88.
- Martin, S.R., and Bayley, P.M. (2004). Calmodulin bridging of IQ motifs in myosin-V. *FEBS Lett.* *567*, 166–170.
- Mccoy, A.J., Grosse-Kunstleve, R.W., Adams, P.D., Winn, M.D., Storoni, L.C., and Read, R.J. (2007). Phaser crystallographic software. *J. Appl. Crystallogr.* *40*, 658–674.
- Mori, M.X., Vander Kooi, C.W., Leahy, D.J., and Yue, D.T. (2008). Crystal structure of the CaV2 IQ domain in complex with Ca<sup>2+</sup>/calmodulin: high-resolution mechanistic implications for channel regulation by Ca<sup>2+</sup>. *Structure* *16*, 607–620.
- Mukherjee, M., Llinas, P., Kim, H., Travaglia, M., Safer, D., Menetrey, J., Franzini-Armstrong, C., Selvin, P.R., Houdusse, A., and Sweeney, H.L. (2009). Myosin VI dimerization triggers an unfolding of a three-helix bundle in order to extend its reach. *Mol. Cell* *35*, 305–315.
- Murshudov, G.N., Skubak, P., Lebedev, A.A., Pannu, N.S., Steiner, R.A., Nicholls, R.A., Winn, M.D., Long, F., and Vagin, A.A. (2011). REFMAC5 for the refinement of macromolecular crystal structures. *Acta Crystallogr. D Biol. Crystallogr.* *67*, 355–367.
- Otwinowski, Z., and Minor, W. (1997). Processing of X-ray diffraction data collected in oscillation mode. *Methods Enzymol.* *276*, 307–326.
- Pan, L., and Zhang, M. (2012). Structures of usher syndrome 1 proteins and their complexes. *Physiology (Bethesda)* *27*, 25–42.
- Parrinello, M., and Rahman, A. (1981). Polymorphic transitions in single-crystals—a new molecular-dynamics method. *J. App. Phys.* *52*, 7182–7190.
- Peckham, M. (2011). Coiled coils and SAH domains in cytoskeletal molecular motors. *Biochem. Soc. Trans.* *39*, 1142–1148.
- Peckham, M., and Knight, P.J. (2009). When a predicted coiled coil is really a single alpha-helix, in myosins and other proteins. *Soft Matter* *5*, 2493–2503.
- Pronk, S., Pall, S., Schulz, R., Larsson, P., Bjelkmar, P., Apostolov, R., Shirts, M.R., Smith, J.C., Kasson, P.M., van der Spoel, D., et al. (2013). GROMACS 4.5: a high-throughput and highly parallel open source molecular simulation toolkit. *Bioinformatics* *29*, 845–854.
- Richardson, G.P., de Monvel, J.B., and Petit, C. (2011). How the genetics of deafness illuminates auditory physiology. *Annu. Rev. Physiol.* *73*, 311–334.
- Ropars, V., Yang, Z., Isabet, T., Blanc, F., Zhou, K., Lin, T., Liu, X., Hissier, P., Samazan, F., Amigues, B., et al. (2016). The myosin X motor is optimized for movement on actin bundles. *Nat. Commun.* *7*, 12456.
- Sakai, T., Umeki, N., Ikebe, R., and Ikebe, M. (2011). Cargo binding activates myosin VIIa motor function in cells. *Proc. Natl. Acad. Sci. USA* *108*, 7028–7033.
- Sakai, T., Jung, H.S., Sato, O., Yamada, M.D., You, D.J., Ikebe, R., and Ikebe, M. (2015). Structure and regulation of the movement of human myosin VIIa. *J. Biol. Chem.* *290*, 17587–17598.
- Sivaramakrishnan, S., and Spudich, J.A. (2011). Systematic control of protein interaction using a modular ER/K alpha-helix linker. *Proc. Natl. Acad. Sci. USA* *108*, 20467–20472.
- Spink, B.J., Sivaramakrishnan, S., Lipfert, J., Doniach, S., and Spudich, J.A. (2008). Long single alpha-helical tail domains bridge the gap between structure and function of myosin VI. *Nat. Struct. Mol. Biol.* *15*, 591–597.
- Swanson, C.J., and Sivaramakrishnan, S. (2014). Harnessing the unique structural properties of isolated alpha-helices. *J. Biol. Chem.* *289*, 25460–25467.
- Tamagawa, Y., Kitamura, K., Ishida, T., Ishikawa, K., Tanaka, H., Tsuji, S., and Nishizawa, M. (1996). A gene for a dominant form of non-syndromic sensorineural deafness (DFNA11) maps within the region containing the DFNB2 recessive deafness gene. *Hum. Mol. Genet.* *5*, 849–852.
- Terwilliger, T.C., Grosse-Kunstleve, R.W., Afonine, P.V., Moriarty, N.W., Zwart, P.H., Hung, L.W., Read, R.J., and Adams, P.D. (2008). Iterative model building, structure refinement and density modification with the PHENIX AutoBuild wizard. *Acta Crystallogr. D Biol. Crystallogr.* *64*, 61–69.
- Tidow, H., and Nissen, P. (2013). Structural diversity of calmodulin binding to its target sites. *FEBS J.* *280*, 5551–5565.
- Tilney, L.G., Tilney, M.S., and DeRosier, D.J. (1992). Actin filaments, stereocilia, and hair cells: how cells count and measure. *Annu. Rev. Cell Biol.* *8*, 257–274.
- Trybus, K.M. (1994). Role of myosin light-chains. *J. Muscle Res. Cell Motil* *15*, 587–594.
- Umeki, N., Jung, H.S., Watanabe, S., Sakai, T., Li, X.D., Ikebe, R., Craig, R., and Ikebe, M. (2009). The tail binds to the head-neck domain, inhibiting ATPase activity of myosin VIIa. *Proc. Natl. Acad. Sci. USA* *106*, 8483–8488.
- UniProt Consortium. (2015). UniProt: a hub for protein information. *Nucleic Acids Res.* *43*, D204–D212.
- Vagin, A., and Teplyakov, A. (1997). MOLREP: an automated program for molecular replacement. *J. Appl. Crystallogr.* *30*, 1022–1025.
- Van Petegem, F., Chatelain, F.C., and Minor, D.L., Jr. (2005). Insights into voltage-gated calcium channel regulation from the structure of the CaV1.2 IQ domain-Ca<sup>2+</sup>/calmodulin complex. *Nat. Struct. Mol. Biol.* *12*, 1108–1115.
- Wang, C., Chung, B.C., Yan, H., Wang, H.G., Lee, S.Y., and Pitt, G.S. (2014). Structural analyses of Ca(2+)-CaM interaction with NaV channel C-termini reveal mechanisms of calcium-dependent regulation. *Nat. Commun.* *5*, 4896.
- Weil, D., Kussel, P., Blanchard, S., Levy, G., LeviAcobas, F., Drira, M., Ayadi, H., and Petit, C. (1997). The autosomal recessive isolated deafness, DFNB2,

- and the Usher 1B syndrome are allelic defects of the myosin-VIIA gene. *Nat. Genet.* **16**, 191–193.
- Well, D., Blanchard, S., Kaplan, J., Guilford, P., Gibson, F., Walsh, J., Mburu, P., Varela, A., Levillers, J., Weston, M.D., et al. (1995). Defective myosin VIIA gene responsible for usher syndrome type 1b. *Nature* **374**, 60–61.
- Winn, M.D., Ballard, C.C., Cowtan, K.D., Dodson, E.J., Emsley, P., Evans, P.R., Keegan, R.M., Krissinel, E.B., Leslie, A.G., McCoy, A., et al. (2011). Overview of the CCP4 suite and current developments. *Acta Crystallogr. D Biol. Crystallogr.* **67**, 235–242.
- Wu, L., Pan, L., Wei, Z., and Zhang, M. (2011). Structure of MyTH4-FERM domains in myosin VIIa tail bound to cargo. *Science* **331**, 757–760.
- Yang, Y., Baboolal, T.G., Siththanandan, V., Chen, M., Walker, M.L., Knight, P.J., Peckham, M., and Sellers, J.R. (2009). A FERM domain autoregulates *Drosophila* myosin 7a activity. *Proc. Natl. Acad. Sci. USA* **106**, 4189–4194.
- Yu, C., Feng, W., Wei, Z., Miyanoiri, Y., Wen, W.Y., Zhao, Y.X., and Zhang, M.J. (2009). Myosin VI undergoes cargo-mediated dimerization. *Cell* **138**, 537–548.
- Yu, C., Lou, J., Wu, J., Pan, L., Feng, W., and Zhang, M. (2012). Membrane-induced lever arm expansion allows myosin VI to walk with large and variable step sizes. *J. Biol. Chem.* **287**, 35021–35035.
- Zhu, T., Beckingham, K., and Ikebe, M. (1998). High affinity  $\text{Ca}^{2+}$  binding sites of calmodulin are critical for the regulation of myosin I beta motor function. *J. Biol. Chem.* **273**, 20481–20486.

## STAR★METHODS

## KEY RESOURCES TABLE

REAGENT or RESOURCE	SOURCE	IDENTIFIER
Chemicals, Peptides, and Recombinant Proteins		
rhodamine-conjugated phalloidin	Invitrogen	Cat#R415
DMEM	Life Technologies	Cat#12800-017
FBS	Hyclone	Cat#SV30160.03
Trypsin	Sigma	Cat#T4665
Synthetic Myo10 IQ3 peptide (LLRRRFLHLKKAIVFQKQLRGQIARRVY)	Synthesized by ChinaPeptides	N/A
Synthetic Myo9a IQ6 peptide (RKKYKEQRNKIILLQSIYRGFRARQRC)	Synthesized by ChinaPeptides	N/A
Synthetic Myo15a IQ3 peptide (RQRYQMRQSLKFRSLVHTYVNRURY)	Synthesized by ChinaPeptides	N/A
Recombinant protein: mouse Myo7a SAH (aa 866-935, ref# NP_001243010.1)	This paper	N/A
Recombinant protein: mouse Myo7a IQ5 (aa 828-870, ref# NP_001243010.1)	This paper	N/A
Recombinant protein: mouse Myo7a IQ5-SAH (aa 828-935, ref# NP_001243010.1)	This paper	N/A
Recombinant protein: human Calmodulin (full length, ref# P62158)	This paper	N/A
Critical Commercial Assays		
NanoJuice transfection kit	Millipore	Cat#71902-4
Deposited Data		
Myo7a 866-935 structure	This paper	PDB: 5WST
Myo7a IQ5-SAH/apo-CaM complex structure	This paper	PDB: 5WSU
Myo7a IQ5/Ca <sup>2+</sup> -CaM complex structure	This paper	PDB: 5WSV
Experimental Models: Cell Lines		
Human: HeLa cells	ATCC	CCL-2
Experimental Models: Organisms/Strains		
<i>Escherichia coli</i> : BL21-CodonPlus	Invitrogen	#230240
Recombinant DNA		
Plasmid: GFP-Myo10	This paper	N/A
Plasmid: GFP-Myo10-(IQ5) <sub>7a</sub>	This paper	N/A
Plasmid: GFP-Myo10-(IQ2) <sub>1c</sub>	This paper	N/A
Software and Algorithms		
Origin7.0	OriginLab	<a href="http://www.originlab.com/">http://www.originlab.com/</a>
GraphPad Prism	GraphPad Software Inc.	<a href="http://www.graphpad.com/scientific-software/prism/">http://www.graphpad.com/scientific-software/prism/</a>
HKL2000	(Otwinowski and Minor, 1997)	<a href="http://www.hkl-xray.com/">http://www.hkl-xray.com/</a>
iMosflm & SCALA	(Winn et al., 2011)	<a href="http://www.ccp4.ac.uk/">www.ccp4.ac.uk/</a>
MOLREP	(Vagin and Teplyakov, 1997)	<a href="http://www.ccp4.ac.uk/">http://www.ccp4.ac.uk/</a>
PHASER	(McCoy et al., 2007)	<a href="http://www.phaser.cimr.cam.ac.uk/">http://www.phaser.cimr.cam.ac.uk/</a>
PHENIX	(Adams et al., 2010)	<a href="http://www.phenix-online.org/">http://www.phenix-online.org/</a>
Buccaneer	(Cowtan, 2006)	<a href="http://www.ccp4.ac.uk/">http://www.ccp4.ac.uk/</a>
Refmac	(Murshudov et al., 2011)	<a href="http://www.ccp4.ac.uk/">http://www.ccp4.ac.uk/</a>
Coot	(Emsley et al., 2010)	<a href="http://www2.mrc-lmb.cam.ac.uk/Personal/pemsley/cool/">http://www2.mrc-lmb.cam.ac.uk/Personal/pemsley/cool/</a>
GROMACS 4.5	(Pronk et al., 2013)	<a href="http://www.gromacs.org/">http://www.gromacs.org/</a>
PyMOL	DeLano Scientific LLC	<a href="http://www.pymol.org/">http://www.pymol.org/</a>
scan4sah	(Gaspari et al., 2012)	<a href="http://csahserver.chem.elte.hu/">http://csahserver.chem.elte.hu/</a>

## CONTACT FOR REAGENT AND RESOURCE SHARING

Further information and requests for reagents may be directed to, and will be fulfilled by the Lead Contact Mingjie Zhang ([mzhang@ust.hk](mailto:mzhang@ust.hk)).

## EXPERIMENTAL MODEL AND SUBJECT DETAILS

### HeLa Cells Culture

HeLa cells (from ATCC) were cultured in DMEM media containing 10% fetal bovine serum (FBS).

## METHOD DETAILS

### Protein Expression and Purification

Various constructs for Myo7a IQ and post-IQ region were created by cloning the corresponding mouse Myo7a (NCBI: NP\_001243010.1) cDNA into a pET-32m3C vector that contains an N-terminal Trx-tag and a (His)<sub>6</sub>-tag. All truncations and point mutations used in the current study were created with the standard PCR-based mutagenesis method and confirmed by DNA sequencing. For heterologous cell expressions, the full-length human Myo10 (NCBI: NP\_036466.2) and its chimeras were cloned into a modified EGFP vector.

Recombinant proteins were expressed in *Escherichia coli* BL21-CodonPlus and protein expression was induced by addition of IPTG at 16 °C. The His-tagged proteins were purified by Ni<sup>2+</sup>-NTA agarose (QIAGEN) affinity chromatography followed by size-exclusion chromatography using the column buffer of 50 mM Tris-HCl, pH 7.8, containing 100 mM NaCl, 1 mM DTT, and 5 mM EDTA (EDTA buffer) or 50 mM Tris-HCl, pH 7.8, containing 100 mM NaCl, 1 mM DTT, and 10 mM CaCl<sub>2</sub> (CaCl<sub>2</sub> buffer).

### Static Light Scattering Analysis

Proteins were loaded on to a Superose 12 (10/300 GL) column (GE Healthcare) equilibrated with EDTA buffer or CaCl<sub>2</sub> buffer. The AKTA FPLC system was coupled to a three-angle light-scattering detector (miniDAWN TREOS, Wyatt technology) and a refractive index detector (Optilab T-rEX, Wyatt technology). The data were recorded and processed by the ASTRA 6.1.2 software (Wyatt Technology).

### Circular Dichroism Spectroscopy

CD spectra of Myo7a-866-935 at a concentration of 1.8 mg/ml in buffer containing 50 mM Tris-HCl, pH 7.8, 100 mM NaCl, 1 mM DTT and 1 mM EDTA were acquired on a JASCO J-815 CD spectropolarimeter at 20 °C using a cell path length of 1 mm. Each spectrum was collected with three scans spanning a spectral window of 200~250 nm. To investigate urea-induced denaturation, CD spectra of Myo7a-866-935 solutions were measured in the presence of different concentrations of urea. Thermal denaturation experiments of Myo7a-IQ5-SAH/CaM complex (concentration at 26 μM) in the presence or absence of Ca<sup>2+</sup> were performed on Chirascan CD spectrometer (Applied Photophysics) from 16~60 °C at a 0.5 °C stepped temperature ramping with a setting time of 30 sec. In both denaturation experiments, the ellipticities at 222 nm were used to calculate the unfolded fraction and plotted as a function of temperature.

### NMR Spectroscopy

Protein samples for NMR experiments were concentrated to ~0.6 mM in 20 mM Tris buffer containing 100 mM NaCl, 1 mM DTT and 5 mM EDTA at pH 7.0 in 90% H<sub>2</sub>O/10% D<sub>2</sub>O. The <sup>1</sup>H-<sup>15</sup>N HSQC spectrum was acquired at 35 °C on a Varian Inova 750 MHz spectrometer.

### Crystallography

All the crystals were obtained by hanging drop or sitting drop vapor diffusion methods at 16 °C. Crystals of Myo7a-866-935 were grown in solution containing 0.2 M ammonium acetate, 0.1 M sodium acetate (pH 4.6) and 30% w/v PEG 4,000. Crystals of Myo7a-IQ5-SAH/apo-CaM complex were grown in solution containing 0.1 M sodium citrate tribasic (pH 5.6), 20% v/v isopropanol and 20% w/v PEG 4,000. Crystals of IQ5/Ca<sup>2+</sup>-CaM were grown in solution containing 0.2 M ammonium sulfate, 0.1 M Bis-Tris (pH 6.5) and 25% w/v PEG 3,500. To obtain KI-derivative, crystals were soaked in crystallization solution with additional 200 mM KI for several minutes. Crystals were soaked in crystallization solution containing additional 25% glycerol or 25% PEG 400 for cryoprotection. All native datasets were collected at the Shanghai Synchrotron Radiation Facility at 100 K at a wavelength at 0.9793 Å. The iodide derivative dataset was collected on a Rigaku RAXIS IV++ imaging-plate system with a MicroMax-007 copper rotating-anode generator. Data were processed and scaled using the MOSFLM and SCALA in the CCP4 suite ([Winn et al., 2011](#)) or HKL2000 ([Otwinowski and Minor, 1997](#)).

Structure of Myo7a-866-935 was solved by combining molecular replacement and single anomalous dispersion methods. First, molecular replacement was performed with the model of a long helix (1L2P) against the native dataset using program PHASER ([McCoy et al., 2007](#)). The model gave high z-scores of only a few solutions in the rotation function search (>6) but low z-scores of many solutions in translation function search (around 5). Initial refinement was performed with PHENIX ([Adams et al., 2010](#)) but failed to improve beyond the R-free value of 0.42. Attempts to locate the position of heavy atoms failed using various methods for the derivative dataset.

However, refinement of the model against the derivative dataset showed several strong densities in the difference map around the helix. Then several iodide atoms were placed in these strong densities. The coordinates of these placed iodides were input into Autosol as heavy atom positions (Adams et al., 2010) for sites refinement and phasing, which resulted in an improved electron density. Model was further improved by Autobuild in PHENIX (Terwilliger et al., 2008). Molecular replacement with the rebuilt model was carried out against the native dataset using PHASER (McCoy et al., 2007). Further manual model building and refinement were completed iteratively using COOT (Emsley et al., 2010) and PHENIX with twin law found using Xtriage in PHENIX (Adams et al., 2010).

The structure of IQ5-SAH/apo-CaM complex was solved by molecular replacement using MOLREP (Vagin and Teplyakov, 1997) and PHASER (McCoy et al., 2007) with models Myo5a-IQ1/CaM (PDB code: 2IX7) and Myo7a-866-935, respectively. Further manual model building and refinement were completed iteratively using COOT (Emsley et al., 2010) and PHENIX with twin law found using Xtriage in PHENIX (Adams et al., 2010).

The structure of Ca<sup>2+</sup>-CaM in complex with IQ5 (828-870) was solved by molecular replacement using PHASER (McCoy et al., 2007) with the model of Ca<sup>2+</sup>-CaM C-lobe (PDB code: 3G43). Initial model improvement was performed by autobuilding using Buccaneer (Cowtan, 2006). Further manual model building and refinement were completed iteratively using COOT (Emsley et al., 2010) and Refmac (Murshudov et al., 2011). The final refinement statistics are summarized in Table 1. All structure figures were prepared by PyMOL (<http://www.pymol.org>).

### Sequence Analysis

Protein sequences of all found mouse myosins were extracted from Swiss-Prot. Only sequences located at the post-IQ regions (~400 residues following the motor domains) were used for analysis by the scan4csah program (<http://csahserver.chem.elte.hu>). Relative scores of best found SAH from each myosin were extracted to construct the bar chart. Score of 2.0 was chosen as the threshold for SAH since SAHs with score lower than 2 turned out to be false positive (i.e. overlapping with the coiled-coil region).

### Trypsin Partial Digestion Studies

Myo7a-IQ5-SAH/CaM complex solution (1 mg/ml) was treated with trypsin (from Sigma) at an enzyme/substrate molar ratio of 1:800 at room temperature in EDTA buffer or CaCl<sub>2</sub> buffer. Aliquots were taken at various time points and stopped by boiling with the sample buffer, and the reaction products were analyzed by SDS/PAGE with Coomassie blue staining.

Similar experimental setting was applied for the analytical gel chromatography analysis. Myo7a-IQ5-SAH/CaM complex (1 mg/ml) was treated with trypsin with the same ratio at room temperature in CaCl<sub>2</sub> buffer. After 45 minutes digestion, both the digested solution and the undigested control were analyzed by analytical size exclusion chromatography with the digestion buffer as the column buffer. Fractionations were also analyzed by SDS/PAGE with Coomassie blue staining.

### Molecular Dynamics Simulations

Two models were built, Myo7a IQ5-SAH/apo-CaM and Myo7a IQ5-SAH/CaM-Ca<sup>2+</sup>. The IQ5/CaM parts were built based on the two complex structure. The backbones of the junctional region and SAH were built based on the IQ5-SAH/apo-CaM structure while the sidechains of the SAH were built based on the 2.1 Å SAH structure. These two models were used as initial structures for MD simulations. For Ca<sup>2+</sup>-CaM system, the structure was solvated in a dodecahedron box with 104,849 TIP3P water molecules (Jorgensen and Madura, 1983). Then, we added 296 Na<sup>+</sup> and 289 Cl<sup>-</sup> ions, to neutralize the system and create a 0.15 M salt concentration environment. For apo-CaM system, the model was solvated in a dodecahedron box with 104,982 TIP3P water molecules, followed by addition of 305 Na<sup>+</sup> and 290 Cl<sup>-</sup> ions to neutralize the system and create a 0.15 M salt concentration environment. For all succeeding steps, GROMACS 4.5 simulation package (Pronk et al., 2013) and AMBER 99SB-ILDN force field (Lindorff-Larsen et al., 2010) were used. Long-range electrostatic interactions were treated by Particle-Mesh Ewald (PME) method (Darden et al., 1993). Electrostatic and van der Waals short-range interactions were calculated using a cutoff of 10 Å. All bonds in protein molecule and water were constrained using LINCS algorithm (Hess et al., 1997).

Following the solvation step, for both systems, energy minimization was performed using steepest descent method. For equilibration, we performed a 100 ps NVT simulation at 300 K using the V-rescale thermostat with a coupling constant of 0.1 ps (Bussi et al., 2007). This is followed by 100 ps NPT equilibration simulation using Parrinello-Rahman (Parrinello and Rahman, 1981) barostat with a coupling constant of 2.0 ps at pressure of 1 bar at 300 K. For these two equilibration simulations, position restraints (with force constant of 1000 kJ mol<sup>-1</sup> nm<sup>-1</sup>) were applied to heavy atoms. For the production, we performed five independent 40 ns NPT simulations for each system starting from different velocities.

### Isothermal Titration Calorimetry Assay

Isothermal titration calorimetry (ITC) measurements were carried out on a VP-ITC Microcal calorimeter (Microcal) at 25 °C. Titration buffer contained 50 mM Tris-HCl, pH 7.8, 100 mM NaCl, 1 mM DTT, containing 5 mM EDTA or 5 mM CaCl<sub>2</sub>. Each titration point was performed by injecting a 10 μL 100 μM CaM into various peptides in the cell at a time interval of 120 seconds to ensure that the titration peak returned to the baseline. The titration data were analyzed by Origin7.0 (Microcal).

### Cellular Localization and Filopodia Quantification

HeLa cells were transiently transfected with 0.5 μg of each plasmid (12-well plate) per well using a NanoJuice transfection kit (Millipore), and cells were cultured for 24 h in DMEM containing 10% FBS in 10% CO<sub>2</sub> before fixation. Cells were imaged with a Nikon

TE2000E inverted fluorescent microscope. Actin was stained with rhodamine-conjugated phalloidin (Invitrogen) to visualize filopodia. The number of GFP puncta at the tips of filopodia were tracked and quantified.

### **QUANTIFICATION AND STATISTICAL ANALYSIS**

Data of filopodia assays were expressed as means  $\pm$  SD from three independent experiments and analyzed using a Student's *t* test, \*\*\**p* < 0.001. Typically, at least 10 cells were quantified for each construct at each experiment. Statistical analysis was performed in GraphPad Prism.

### **DATA AND SOFTWARE AVAILABILITY**

The atomic coordinates of Myo7a-866-935, Myo7a-IQ5-SAH/apo-CaM complex and Myo7a-IQ5/Ca<sup>2+</sup>-CaM complex reported in this paper are deposited to the Protein Data Bank under accession codes of PDB: 5WST, 5WSU, and 5WSV, respectively.